Spectrochimica Acta Part A: Molecular and Biomolecular Spectroscopy 346 (2026) 126870

Contents lists available at ScienceDirect

Spectrochimica Acta Part A:
Molecular and Biomolecular Spectroscopy

journal homepage: www.journals.elsevier.com/spectrochimica-acta-part-a-molecular-and-biomolecular-spectroscopy

Anomalous $^5D_0 \rightarrow {}^7F_4$ transition induced by alkali ion co-doping in Eu^{3+}-activated $K_7SrY_2(B_5O_{10})_3$ borates: A Judd–Ofelt and photoluminescence analysis for pc-WLEDs

Abeer S. Altowyan [a], S. Cam Kaynar [b], H. Aydin [c,d], U.H. Kaynar [e], M.B. Coban [f], Jabir Hakami [g], A. Canimoglu [h], Y. Ozcan [i], N. Can [g,j,*]

[a] Department of Physics, College of Science, Princess Nourah bint Abdulrahman University, P.O. Box 84428, Riyadh 11671, Saudi Arabia
[b] Manisa Celal Bayar University, Faculty of Engineering and Natural Sciences, Physics Department, Manisa, Turkey
[c] Graphene Application & Research Center, Izmir Katip Celebi University, Izmir, Turkey
[d] Central Research Laboratories, Izmir Katip Celebi University, Izmir, Turkey
[e] Bakırcay University, Faculty of Engineering and Architecture, Department of Fundamental Sciences, Menemen, Izmir, Turkey
[f] Balikesir University, Faculty of Arts and Sciences, Department of Physics, Balikesir, Turkey
[g] Jazan University, College of Science, Department of Physical Sciences, Physics Division, P.O. Box 114, 45142 Jazan, Saudi Arabia
[h] Nigde Omer Halisdemir University, Faculty of Science, Physics Department, Nigde, Turkey
[i] Department of Biomedical Engineering, Faculty of Technology, Pamukkale University, 20070 Denizli, Turkey
[j] Nanotechnology Research Unit, College of Science, Jazan University, P.O. Box. 114, Jazan 45142, Saudi Arabia

HIGHLIGHTS

- Li^+ co-doping boosted the $^5D_0 \rightarrow {}^7F_4$ red emission ~58× under 392 nm excitation.
- High Ω_6 value from Judd–Ofelt analysis indicates strong dipole transitions.
- KSYBO:Eu^{3+},Li^+ shows 97.7 % color purity and 2253 K CCT for red phosphors.
- Li^+-induced lattice distortion activates forbidden transitions, shifts to red.

GRAPHICAL ABSTRACT

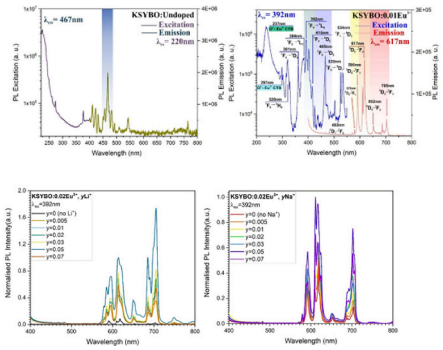

ARTICLE INFO

Keywords:
Eu^{3+} phosphor
$K_7SrY_2(B_5O_{10})_3$
Chromaticity coordinates
Judd–Ofelt analysis
Lattice distortion
Anomalous red emission

ABSTRACT

In this study, red-emitting $K_7SrY_2(B_5O_{10})_3$:Eu^{3+} phosphors were synthesized via high-temperature solid-state reaction. The effects of Li^+ and Na^+ co-doping on structural and photoluminescent properties were investigated. XRD and Rietveld refinement confirmed a phase-pure trigonal structure. Under 394 nm excitation, Li^+ co-doping induced significant local lattice asymmetry, leading to a remarkable ~58-fold enhancement of $^5D_0 \rightarrow {}^7F_4$ transition, which is typically parity-forbidden. This behavior is further supported by the high Judd–Ofelt Ω_6 parameter (5.42×10^{-20} cm^2), indicating enhanced electric dipole character due to symmetry breaking. CIE chromaticity coordinates shifted toward deeper red emission with color purity up to 97.7 % and CCT as low as

* Corresponding author at: Jazan University, College of Science, Department of Physical Sciences, Physics Division, P.O. Box 114, 45142 Jazan, Saudi Arabia.
E-mail address: ncan@jazanu.edu.sa (N. Can).

https://doi.org/10.1016/j.saa.2025.126870
Received 29 June 2025; Received in revised form 23 July 2025; Accepted 25 August 2025
Available online 26 August 2025

2253 K. Temperature-dependent PL confirmed high thermal stability (E_a = 0.190 eV). These results demonstrate that Li^+-induced symmetry distortion is a powerful strategy to enhance anomalous red emission, positioning KSYBO:Eu^{3+},Li^+ as a promising red phosphor for pc-WLEDs.

1. Introduction

Rare-earth (RE) ion-activated phosphors are cornerstone materials in solid-state lighting, optical displays, and photonic applications due to their sharp emission lines, high quantum efficiency, and robust thermal stability [1,2]. The 4f–4f electronic transitions of trivalent rare-earth ions are highly shielded by outer 5 s and 5p orbitals, resulting in narrow-band emissions that are largely insensitive to the surrounding crystal field, thereby ensuring excellent spectral purity across the UV to near-infrared range [3]. Among these ions, Eu^{3+} is widely favored for red emission, particularly due to its hypersensitive $^5D_0 \rightarrow {}^7F_2$ transition, which is highly responsive to the asymmetry of the local crystal field [4,5].

Developing red phosphors that are both efficient and thermally stable under near-UV excitation has become a central challenge in photonics. Oxide-based host lattices have emerged as favorable candidates, as they can effectively accommodate RE^{3+} ions while minimizing non-radiative losses. Although borates possess relatively high phonon energies (~1350–1400 cm^{-1}), they remain attractive host materials owing to their excellent structural tunability, resistance to thermal degration, and capability to stabilize diverse rare-earth dopants [6–9]. These structural features suppress multiphonon relaxation processes and allow for high radiative efficiency even under elevated thermal conditions [10,11].

Several borate-based compounds have recently emerged as promising rare-earth hosts, including the $K_7MeR_2(B_5O_{10})_3$ (Me = Ca, Sr; R = Y, RE) [12–16], $MMeRB_6O_{12}$ [17,18], and $LiCaR_5(BO_3)_6$ [19–21] families, each providing unique structural motifs that support efficient rare-earth ion incorporation.

Among these, $K_7SrY_2(B_5O_{10})_3$ (KSYBO) stands out due to its R32 symmetry and ability to stabilize Tb^{3+}-based luminescence efficiently. Given this success, Eu^{3+}—another symmetry-sensitive ion critical for red-emission—emerges as a logical next dopant to explore [22]. In their study, the incorporation of alkali co-dopants (Li^+/Na^+) was found to modulate the local crystal field and reduce non-radiative recombination, leading to a more than tenfold enhancement in green emission and a substantial increase in photoluminescence lifetime.

Eu^{3+}, a trivalent rare-earth ion with strong sensitivity to local symmetry, has already demonstrated promising luminescence behavior in structurally related borate hosts [23]. Given the success of Tb^{3+} doping in KSYBO, this raises the question of whether a similarly favorable environment can be achieved for red-emitting Eu^{3+} ions in the same lattice. Notably, no prior studies have investigated Eu^{3+} doping in the KSYBO lattice, despite the proven success of Tb^{3+} incorporation in the same host. This presents a clear research gap, especially given Eu^{3+}'s sensitivity to local symmetry and its pivotal role in red phosphor emission. These factors strengthen the case for using trigonal borates like KSYBO, which offer multi-cationic flexibility, oxidation resistance, and favorable coordination environments.

To further enhance the luminescent properties of Eu^{3+} in such host lattices, co-doping strategies involving alkali ions such as Li^+ and Na^+ have received growing attention. This trend is supported by several recent studies reporting enhanced photoluminescence performance upon Li^+/Na^+ co-doping. Eu^{3+} ions, with their strong sensitivity to local symmetry, stand to benefit significantly from the low-symmetry Y^{3+} sites present in the KSYBO structure. Moreover, the host's demonstrated capacity to accommodate RE^{3+} ions without inducing phase transitions or secondary phases makes it a compelling candidate for further exploration. Several studies have demonstrated that doping with Li^+ and Na + ions can significantly influence the luminescent properties of rare-earth (RE)-activated systems [24–27]. According to quantum mechanical selection rules, the intra-4f transitions of RE ions are generally parity-forbidden [28]. However, these rules can be relaxed due to the mixing of 4f states with higher-lying electronic configurations, allowing for weak electric dipole transitions. Li^+ ions, due to their small ionic radius, are increasingly recognized as effective modifiers of the local crystal structure around RE ions. They can occupy substitutional or interstitial sites within the host lattice, leading to changes in local symmetry and field strength, which in turn can enhance luminescence performance. In addition to enhancing radiative transitions, the symmetry breaking caused by alkali ion incorporation can suppress non-radiative multiphonon relaxation pathways by reducing parity-forbidden transition restrictions. Furthermore, the Judd–Ofelt (J–O) theory provides a robust framework for interpreting the optical transitions of RE ions in crystalline environments [29–31]. The theory introduces three phenomenological intensity parameters (Ω_2, Ω_4, and Ω_6), which quantify the strengths of electric dipole transitions between 4f levels. These parameters are intimately linked to the local crystal field and are essential for understanding the radiative transition probabilities and the electronic structure of 4f states in RE ions.

In this work, we present for the first time a comprehensive synthesis and photoluminescence analysis of Eu^{3+}-activated $K_7SrY_2(B_5O_{10})_3$ phosphors. Through structural, spectroscopic, and chromaticity-based evaluation, we aim to elucidate the suitability of KSYBO as a red-emitting component for phosphor-converted white LEDs and photonic applications. Our findings are contextualized by comparative assessment with existing RE^{3+}-activated borates, and the results provide novel insights into the role of lattice symmetry and coordination chemistry in tuning Eu^{3+} emission properties.

2. Experimental methods

2.1. Materials and synthesis protocol

The synthesis of the $K_7SrY_2(B_5O_{10})_3$ (KSYBO) phosphor matrix was carried out using analytical-grade precursors: potassium carbonate (K_2CO_3), strontium carbonate ($SrCO_3$), and boric acid (H_3BO_3) obtained from Sigma–Aldrich (≥99.9 %). Europium oxide (Eu_2O_3, 99.99 %, Alfa Aesar) served as the luminescent activator, substituting the Y^{3+} site in varying concentrations (0.5–7 wt%) to evaluate its impact on structural and photonic behavior. To investigate alkali co-doping effects, lithium carbonate (Li_2CO_3) and sodium carbonate (Na_2CO_3) were introduced in controlled amounts (0.5–3.0 wt%) as charge compensators and lattice modifiers.

Accurate stoichiometric ratios of all raw materials were weighed and thoroughly ground in an agate mortar with minimal deionized water, yielding a homogeneous slurry. The mixture was then dried at 120 °C and subjected to a conventional ceramic solid-state reaction technique. The dried powders underwent pre-calcination at 600 °C for 4 h to eliminate volatile by-products and initiate decomposition reactions. The intermediate product was re-ground and subsequently annealed at 950 °C for 6 h in ambient air to achieve complete crystallization. After slow cooling, all samples were preserved in airtight containers to prevent moisture absorption.

This route facilitated efficient incorporation of Eu^{3+} ions and alkali co-dopants into the borate lattice, enabling the formation of phase-pure, highly crystalline phosphors suitable for subsequent structural and optical characterization.

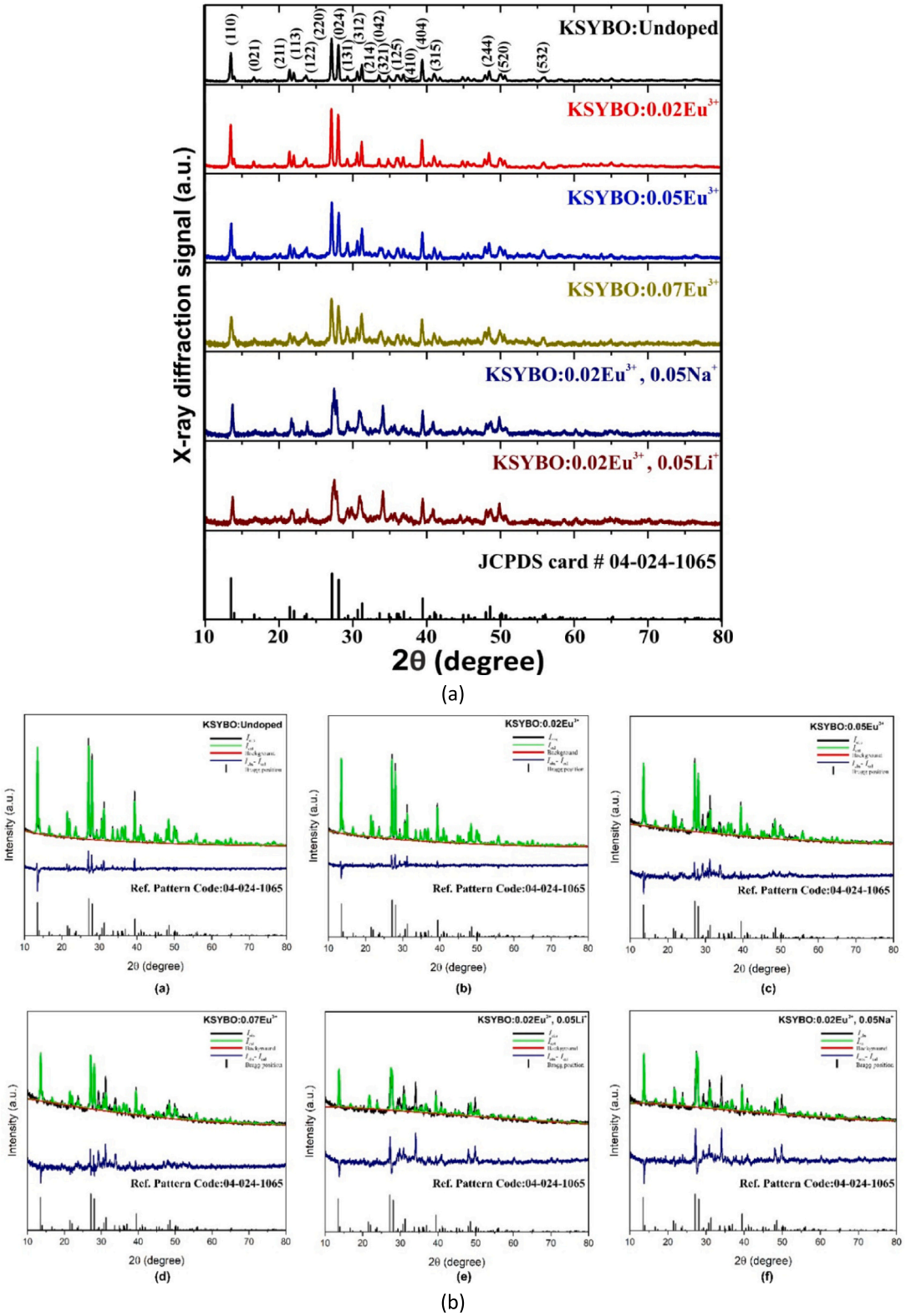

Fig. 1. (a) X-ray diffraction (XRD) patterns of undoped and Eu^{3+}-doped $K_7SrY_2(B_5O_{10})_3$ samples, including alkali ion co-doped compositions. All peaks correspond to the trigonal R32 phase, consistent with JCPDS card #04-024-1065. (b) Rietveld refinement profiles of undoped and Eu^{3+}/alkali-doped KSYBO samples. Experimental (green), calculated (red), and difference (blue) curves demonstrate high-quality fitting and phase purity with reference code 04–024-1065. (c) Polyhedral representations of the local oxygen coordination environments surrounding Y^{3+}, Sr^{2+}, and the three non-equivalent K^+ sites (K1, K2, and K3) in the trigonal $K_7SrY_2(B_5O_{10})_3$ lattice. (For interpretation of the references to color in this figure legend, the reader is referred to the web version of this article.)

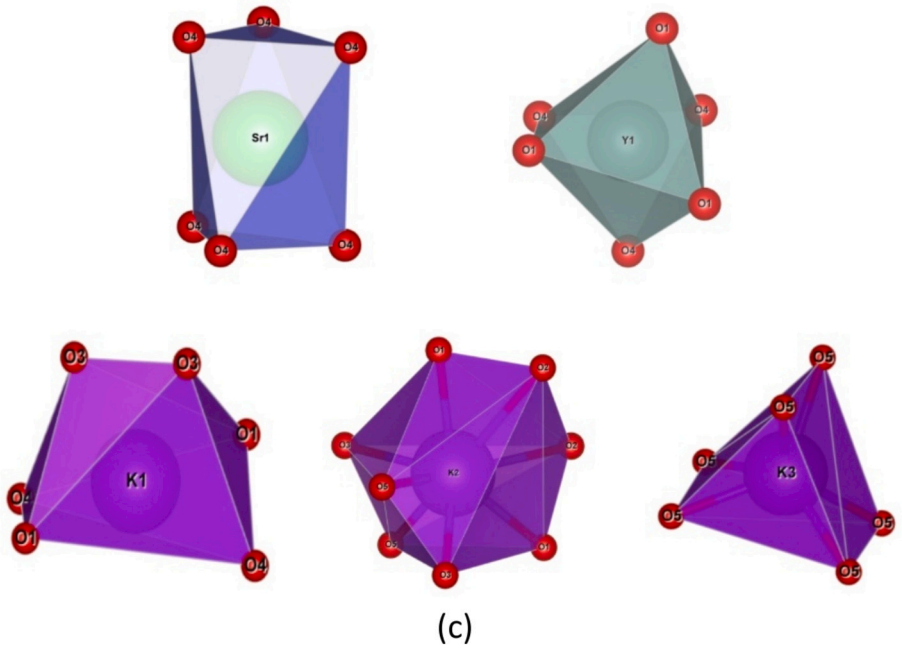

Fig. 1. (*continued*).

2.2. Characterization techniques

The synthesized materials were comprehensively characterized using a suite of analytical techniques to investigate their structural, vibrational, morphological, and luminescent properties. Phase identification and crystallographic analysis were conducted via powder X-ray diffraction (XRD) using a Malvern Panalytical Empyrean diffractometer equipped with CuKα radiation (λ = 1.5406 Å). Diffraction patterns were collected over a 2θ range of 10°–80° and refined using the Rietveld method implemented in HighScore Plus software.

Fourier-transform infrared (FTIR) spectroscopy (Thermo Scientific Nicolet iS50, 4000–400 cm^{-1}) was used to identify functional groups and assess borate vibrational modes. Raman spectra were recorded using a Renishaw inVia system with a 532 nm laser, providing complementary insights into the BO_3/BO_4 network and local structural distortions.

Surface morphology and compositional homogeneity were evaluated using scanning electron microscopy (SEM, ZEISS GeminiSEM 500) coupled with energy-dispersive X-ray spectroscopy (EDS). Samples were sputter-coated with gold to mitigate surface charging during imaging.

Photoluminescence (PL) excitation and emission spectra were measured using an Edinburgh FS5 spectrofluorometer (150 W xenon arc lamp). Time-resolved PL decay measurements were also performed to probe radiative dynamics. The chromatic performance was analyzed via CIE 1931 chromaticity coordinates, and Judd–Ofelt theoretical modeling was applied to quantify radiative transition probabilities and asymmetry parameters associated with Eu^{3+} sites.

3. Results and discussions

3.1. Phase structure and substitutional behavior of Eu^{3+} ions

The phase purity and structural integrity of the synthesized $K_7SrY_2(B_5O_{10})_3$ (KSYBO) phosphors, doped with varying concentrations of Eu^{3+} and co-doped with alkali ions (Li^+ and Na^+), were comprehensively examined using powder X-ray diffraction (XRD). As depicted in Fig. 1a, all samples exhibit well-resolved diffraction peaks that align closely with the standard pattern indexed to the trigonal phase (space group *R32*) corresponding to JCPDS Card #04–024-1065, confirming the formation of a single-phase crystalline lattice without secondary impurity phases [22].

To further quantify the structural evolution, Rietveld refinements were performed on the XRD patterns (Fig. 1b). The refined profiles demonstrate excellent agreement between experimental and simulated data, with low residual values (e.g., $R_{wp} \leq 0.108$ and $\chi^2 \leq 3.77$), as summarized in Table 1. The refinement reliability factors (R_{wp}, R_p, and χ^2) remained within acceptable limits, confirming the robustness of the trigonal phase and validating the structural model. Notably, the unit cell parameters show a gradual increase with rising Eu^{3+} concentration—from $a = b = 13.165$ Å and $c = 15.359$ Å for 2 wt% Eu^{3+}, to $a = b = 13.206$ Å and $c = 15.405$ Å at 7 wt%—suggesting a successful substitutional incorporation of Eu^{3+} into the host lattice. The linear increase in lattice parameters with increasing Eu^{3+} concentration indicates a homogeneous substitutional mechanism without secondary phase formation or phase transition. To further illustrate the local environments of the cation sites, the oxygen coordination geometries around Y^{3+}, Sr^{2+}, and the three non-equivalent K^+ sites (K1, K2, and K3) are visualized in Fig. 1c. These polyhedral representations highlight the distinct local symmetry and coordination numbers that influence Eu^{3+} substitution and the resulting photoluminescent behavior. Based on the refined Rietveld parameters, Eu^{3+} ions are presumed to substitute Y^{3+} sites, which occupy low-symmetry crystallographic positions. This environment allows electric dipole transitions to become partially allowed. For the 2 wt% Eu_2O_3-doped sample, corresponding to ~5.2 mol % Eu^{3+}, the estimated Eu^{3+} ion concentration is $\sim 2.72 \times 10^{22}$ ions/cm^3, calculated from the refined unit cell volume of 2305.6 $Å^3$.

The observed lattice expansion can be rationalized by the slight mismatch between the ionic radii of the dopant and host cation. Eu^{3+} (0.947 Å, CN = 6) is marginally larger than Y^{3+} (0.96 Å, CN = 6), implying a tolerable substitution. To validate this, the ionic radius mismatch percentage (D_r) was calculated using [32]:

$$D_r = \left| \frac{R_m(CN) - R_d(CN)}{R_m(CN)} \right| \times 100\% \quad (1)$$

The calculated D_r values for possible host cations are:

- Y^{3+} site: 1.35 %
- Sr^{2+} site: 19.74 %
- K^+ site: 31.37 %

Table 1
Refined lattice parameters, unit cell volumes, and Rietveld reliability factors of KSYBO samples doped with Eu^{3+} and co-doped with Li^+/Na^+ ions.

	KSYBO					
Unit Cell	Undoped	$0.02Eu^{3+}$	$0.05Eu^{3+}$	$0.07Eu^{3+}$	$0.02Eu^{3+}$,$0.05Li^+$	$0.02Eu^{3+}$,$0.05Na^+$
a [Å]	13.160	13.165	13.181	13.206	13.016	13.0161
b [Å]	13.160	13.165	13.181	13.206	13.016	13.0161
c [Å]	15.358	15.359	15.372	15.405	15.697	15.680
α,β,γ [°]	90, 90, 120	90, 90, 120	90, 90, 120	90, 90, 120	90, 90, 120	90, 90, 120
Vol. [$Å^3$]	2303.674	2305.58	2313.064	2327.026	2303.102	2300.695
χ^2	2.498	2.176	2.759	2.660	3.772	3.683
R_p	0.055	0.050	0.059	0.059	0.078	0.070
R_{wp}	0.076	0.066	0.079	0.079	0.108	0.101
R_{exp}	0.030	0.030	0.028	0.029	0.028	0.027

Since values below 30 % are considered structurally favorable [33], the data strongly support that Eu^{3+} ions preferentially substitute Y^{3+} in the KSYBO lattice. The substitution at Sr^{2+} sites is theoretically possible but less favorable due to higher mismatch, while K^+ positions are structurally incompatible due to excessive deviation.

Interestingly, samples co-doped with Li^+ and Na^+ ions (e.g., KSYBO:$0.02Eu^{3+}$,$0.05Li^+$) exhibit a subtle contraction in unit cell volume (from ~2313.06 to ~2300.7 $Å^3$), which is attributed to the smaller size and aliovalent nature of these monovalent ions. The observed lattice contraction modulates the local crystal environment. Their incorporation likely induces oxygen vacancies or lattice strain, not necessarily for charge compensation, but rather to enhance the crystal field asymmetry and influence Eu^{3+} luminescence behavior.

Overall, the structural data confirm that the KSYBO host lattice maintains its crystallographic stability upon Eu^{3+} doping and alkali co-doping. These observations are indicative of a chemically flexible and structurally tolerant framework, suitable for rare-earth ion incorporation without phase destabilization.

3.2. Microstructural analysis via crystallite size and strain evaluation

In order to better understand the structural alterations arising from Eu^{3+} incorporation and alkali ion co-doping in the KSYBO matrix, parameters such as crystallite size (D), lattice strain (ε), and dislocation density (δ) were calculated through both the Debye–Scherrer approach and the Williamson–Hall (W—H) analysis as introduced by Williamson and Hall [34].

Fig. 2 displays the W—H plots for all samples, where βcosθ is plotted against 4sinθ for multiple Bragg reflections. The linearity of the plots indicates that the observed peak broadening arises from a combined effect of both size and strain contributions. The intercept of the fitted line provides an estimate of crystallite size, while the slope yields the lattice strain.

As summarized in Table 2, the undoped KSYBO sample exhibits a crystallite size of 68 nm (Scherrer) and 64 nm (W—H), with a moderate microstrain value of 2.41×10^{-2} [35]. Upon Eu^{3+} doping, a gradual increase in crystallite size is observed—from 69 nm ($0.02Eu^{3+}$) to 72 nm ($0.07Eu^{3+}$) according to the Scherrer method—suggesting that Eu^{3+} incorporation facilitates grain coalescence and slightly enhances crystallinity.

However, the introduction of Li^+ and Na^+ ions as co-dopants results in a noticeable reduction in crystallite size (down to 57–59 nm) and a corresponding increase in both lattice strain (ε) and dislocation density (δ). This trend suggests enhanced structural distortion, likely arising from ionic radius mismatch and charge imbalance between the monovalent alkali ions and the host cation [35]. These distortions may lead to defect formation and localized lattice stress, as also supported by the increased peak broadening observed in the XRD patterns. This behavior is attributed to the aliovalent nature and smaller ionic radii of Li^+ (0.76 Å) and Na^+ (1.02 Å), which introduce local structural distortion and hinder grain growth. These co-dopants likely induce internal strain via charge compensation and lattice mismatch, contributing to enhanced peak broadening. The microstrain (ε), derived from Williamson–Hall analysis, is a dimensionless parameter that reflects local lattice distortions and internal stress. The observed decrease from 2.41 in the undoped sample to 1.89 in the 0.02Eu,0.05Li-doped sample suggests that Li^+ incorporation alleviates strain by partially stabilizing the lattice framework.

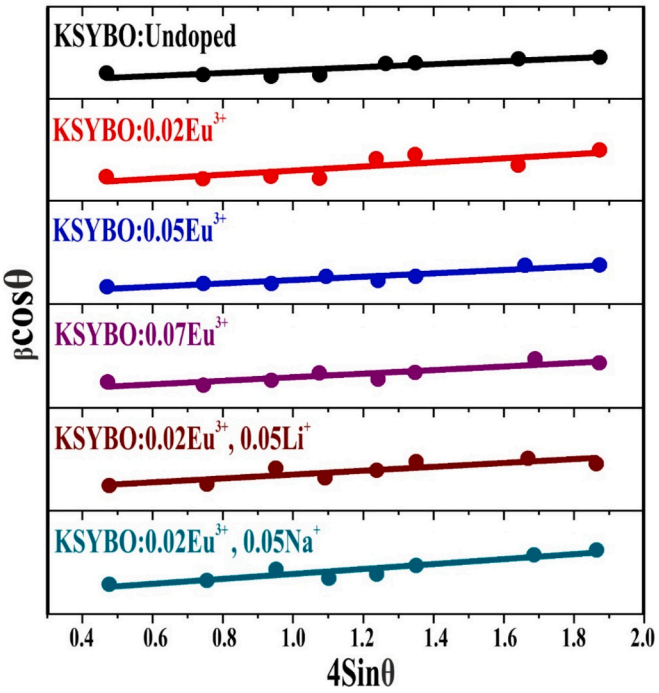

Fig. 2. Williamson–Hall plots (βcosθ vs. 4sinθ) of KSYBO phosphors with different Eu^{3+} doping concentrations and co-doping with Li^+ and Na^+ ions.

Furthermore, the W—H derived crystallite sizes are consistently slightly lower than those obtained from the Scherrer equation, as expected, due to the inclusion of strain-related broadening. This dual-method approach provides a more comprehensive assessment of the microstructural dynamics.

Overall, the microstructural data confirm that Eu^{3+} doping improves crystallinity, while Li^+ and Na^+ co-doping introduce manageable strain and defect levels, potentially influencing luminescence behavior in later sections.

3.3. Morphological and elemental analysis of KSYBO and Eu^{3+}-doped KSYBO phosphors

To investigate the surface morphology and elemental composition of the synthesized phosphors, SEM and EDS analyses were carried out for both undoped KSYBO and KSYBO:$0.02Eu^{3+}$ samples. The SEM

Table 2
Crystallite size (D), dislocation density (δ), and microstrain (ε) of KSYBO samples with varying Eu^{3+} doping concentrations and co-doping with Li^{+} and Na^{+} ions.

Concentration		Undoped	$0.02Eu^{3+}$	$0.05Eu^{3+}$	$0.07Eu^{3+}$	$0.02Eu^{3+}$,$0.05Li^{+}$	$0.02Eu^{3+}$,$0.05Na^{+}$
Scherrer	D (nm)	68	69	71	72	57	59
	$\delta \times 10^{-3}$ (nm^{-2})	0.2180	0.2075	0.1998	0.1945	0.3112	0.2873
Williamson-Hall	D (nm)	64	67	68	69	55	58
	$\varepsilon \times 10^{-2}$	2.41	2.44	2.55	1.54	1.89	2.41

micrographs, embedded within the EDS spectra in Fig. 3(a–b), reveal that both samples exhibit highly porous microstructures with interconnected grains, which are advantageous for enhancing light scattering and potential optical performance in photonic applications.

The EDS spectrum of the undoped KSYBO sample [Fig. 3(a)] confirms the presence of the constituent elements B, O, Sr, Y, and K, in accordance with the nominal chemical formula of $K_7SrY_2(B_5O_{10})_3$. The atomic and weight percentages derived from the EDS quantitative analysis validate the stoichiometric incorporation of these elements.

Upon Eu^{3+} doping [Fig. 3(b)], additional peaks corresponding to Eu^{3+} are clearly observed between 5.5 and 7.5 keV, confirming the successful substitution of Eu^{3+} ions into the host lattice. The elemental quantification reveals an Eu content of approximately 2.57 wt% (0.59 at.%), consistent with the nominal doping level of 0.02. Notably, a slight decrease in B, O, and K content is observed, which may indicate minor lattice adjustments due to the incorporation of the larger Eu^{3+} ion compared to Y^{3+}.

These results collectively confirm the homogeneous distribution of Eu^{3+} ions in the host lattice without the formation of secondary phases, aligning with the XRD findings. The porous morphology and elemental homogeneity suggest the suitability of the KSYBO:Eu^{3+} system for efficient photoluminescent performance.

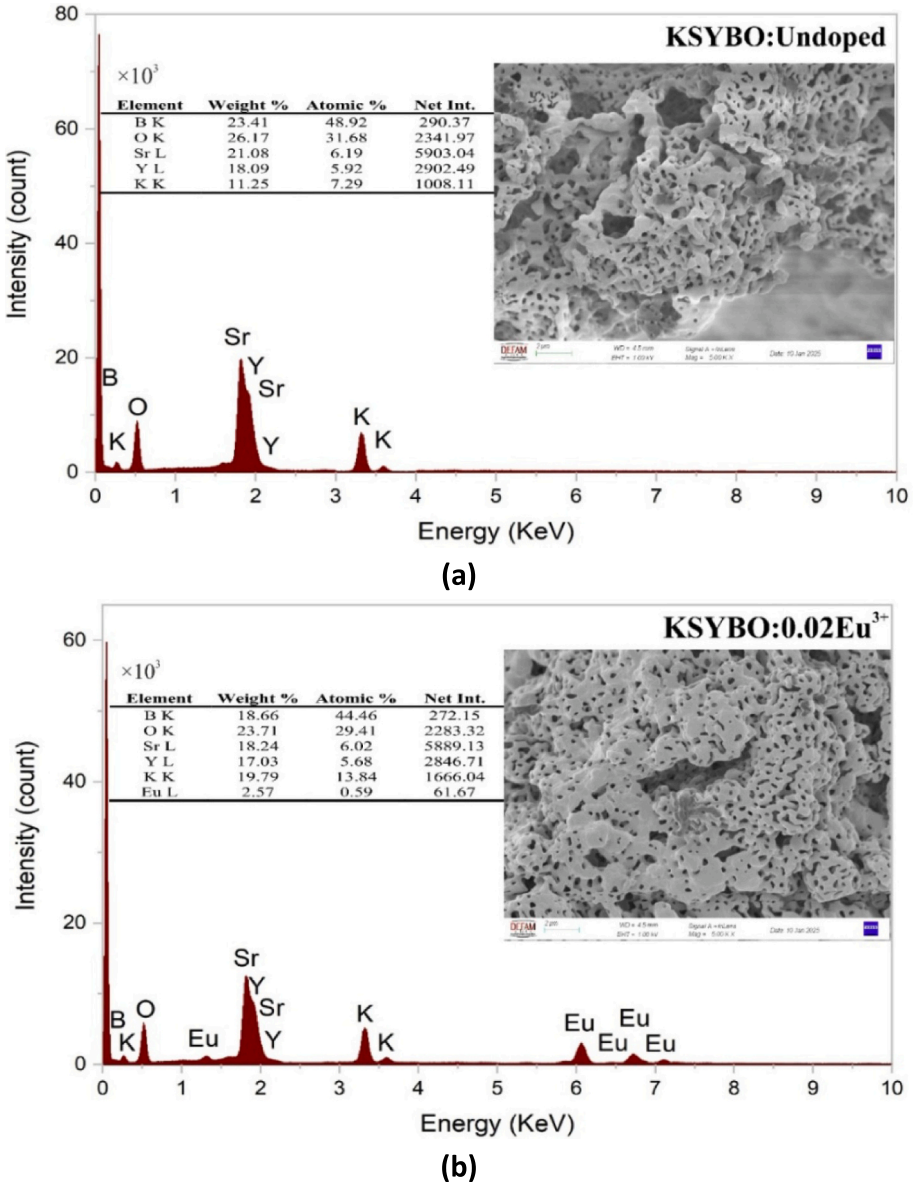

Fig. 3. SEM micrographs and corresponding EDS spectra of (a) undoped KSYBO and (b) KSYBO:0.02Eu^{3+} phosphors.

3.4. FTIR and Raman spectroscopy analysis

FTIR and Raman spectroscopy were employed to investigate the vibrational features and local structure of KSYBO samples, both undoped and doped with Eu^{3+}, with further co-doping using alkali ions (Li^+ and Na^+). The comparison of FTIR and Raman spectra provides a coherent understanding of structural evolution within the borate framework.

In the FTIR spectra (Fig. 4a), a broad absorption band observed in the range of 3400–3200 cm^{-1} is assigned to the stretching vibrations of O—H bonds, indicative of adsorbed water or hydroxyl groups on the particle surfaces [11,36,37]. This feature shows minor variation in intensity upon doping, particularly in the Li^+ co-doped sample, potentially reflecting differences in hydroxyl bonding environments due to local lattice disruptions.

The spectral range between 1350 and 400 cm^{-1} exhibits characteristic absorption bands of borate groups. Peaks at approximately 1356, 1244, and 1193 cm^{-1} correspond to the asymmetric stretching modes of trigonal $[BO_3]^{3-}$ units, while those at 1031, 989, and 937 cm^{-1} are attributed to asymmetric stretching vibrations of tetrahedral $[BO_4]^-$ units [24,38]. This coexistence of $[BO_3]$ and $[BO_4]$ species aligns with the known structural complexity of rare-earth borates, where network connectivity can be modulated by the nature and concentration of dopants [11,38].

Further absorption features near 860, 778, 735, and 615 cm^{-1} are ascribed to bending vibrations of borate linkages and stretching of Y—O bonds. The peak around 494 cm^{-1} also suggests Y—O bond contributions. Upon Eu^{3+} doping and alkali ion incorporation, subtle changes in band positions and intensities are observed, suggesting minor distortions in the local coordination environment [39].

Complementary insights are obtained from the Raman spectra (Fig. 4b). The undoped KSYBO sample displays well-resolved peaks near 934 and 750 cm^{-1}, corresponding to symmetric stretching of $[BO_4]^-$ and bending of $[BO_3]^{3-}$ groups, respectively. These vibrational assignments are consistent with previous Raman studies of borate glasses, where BO_4 and BO_3 units exhibit characteristic features near ~935 and ~ 750 cm^{-1}, as reported in rare-earth-doped oxyfluoride glass ceramics [40] and other borate frameworks [41]. With Eu^{3+} doping, peak broadening and slight shifts are evident, especially in the higher frequency region (1320–1500 cm^{-1}), which may indicate increased structural disorder or modification in bond polarizability due to the incorporation of larger lanthanide ions. Li^+ co-doping further amplifies these distortions, with additional broad features emerging in the 2500–2700 cm^{-1} range. These are not typical phonon modes and may be attributed to second-order Raman processes, such as overtone or combination bands of borate units. However, since they appear only in Eu^{3+}-doped samples and coincide with known Eu^{3+} 4f–4f absorption transitions (e.g. $^7F_0 \rightarrow {}^5D_1$, $^5D_2$) under 532 nm excitation, a resonant Raman enhancement or Eu^{3+}-related luminescence reabsorption contribution is likely. Resonance Raman processes are known to strongly enhance overtone and combination bands when the excitation laser is tuned near an electronic absorption band, particularly in rare-earth systems (e.g., up to $10^6\times$ amplification) [42,43]. Overall, the agreement between FTIR and Raman data — both showing the presence of $[BO_3]$ and $[BO_4]$ species and the dopant-induced modifications — suggests a coherent picture of structural perturbation. These spectroscopic alterations are typical of rare-earth and alkali co-doped borate matrices and reflect trends observed in earlier studies on structurally analogous systems.

3.5. Photoluminescence properties of KSYBO:0.01Eu^{3+} phosphor under different excitation wavelengths

Prior to analysing the doped phosphors, the optical activity of the undoped KSYBO host was examined to confirm the absence of intrinsic or contaminant-related luminescence.

Photoluminescence excitation and emission spectra of the undoped KSYBO matrix were recorded under identical conditions (see Fig. 5a). The emission spectrum does not exhibit any characteristic lines in the

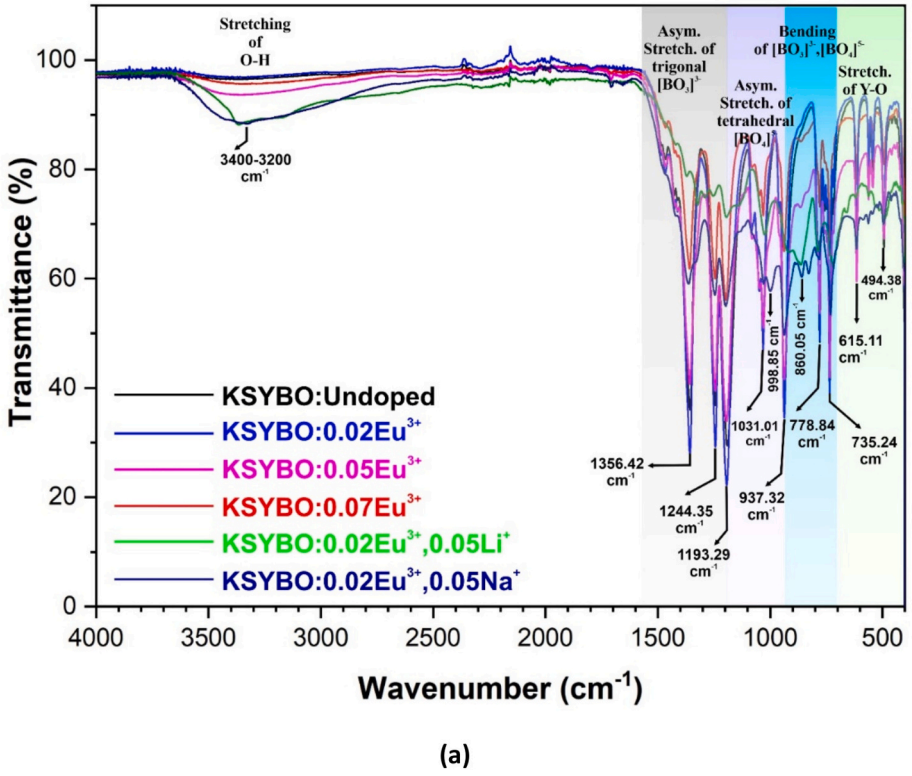

Fig. 4. (a) FTIR spectra of undoped and Eu^{3+}-doped KSYBO phosphors, showing vibrational modes associated with $[BO_3]^{3-}$ and $[BO_4]^{5-}$ groups as well as Y—O bonds. (b) Raman spectra of the same samples, highlighting the structural evolution in borate units upon Eu^{3+} doping and alkali ion incorporation.

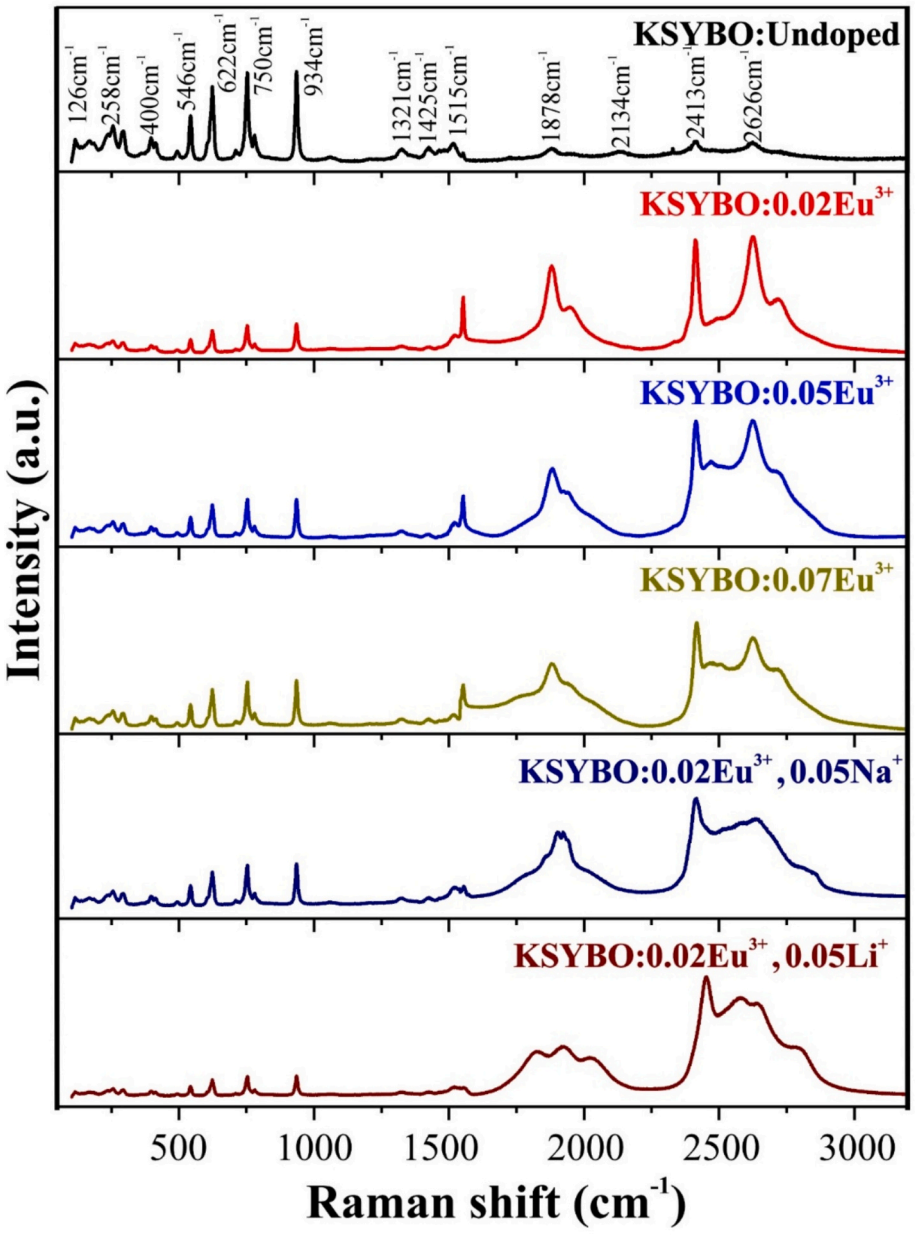

(b)

Fig. 4. (*continued*).

570–720 nm region, particularly at ~617 nm and ~ 705 nm, where Eu^{3+} transitions ($^5D_0 \rightarrow {}^7F_2$ and $^5D_0 \rightarrow {}^7F_4$) are expected. The excitation profile displays a broad band below 300 nm, consistent with host-related absorption (e.g., BO_3 and BO_4 vibrational modes), but no charge transfer or 4f–4f bands related to Eu^{3+}. These findings confirm that the KSYBO host is optically inactive in the relevant range, and all luminescence features in the doped samples originate exclusively from the Eu^{3+} activator. The photoluminescence (PL) excitation and emission spectra of the $K_7SrY_2(B_5O_{10})_3$:0.01Eu^{3+} (KSYBO:0.01Eu^{3+}) phosphor were systematically investigated to elucidate the optical behavior of Eu^{3+} ions within the borate host lattice. Fig. 5b presents both the excitation spectrum (monitored at 617 nm) and the corresponding emission spectrum (excited at 392 nm).

The excitation spectrum reveals several sharp and well-defined peaks characteristic of intra-4f transitions of Eu^{3+} ions. Notably, the most intense excitation band is observed at 392 nm, corresponding to the $^7F_0 \rightarrow {}^5L_6$ transition, which is commonly known as the most efficient channel for exciting Eu^{3+} ions due to its relatively strong electric dipole allowed nature in asymmetrical sites. In addition to these narrow intra-4f bands, broad excitation features centered around 297 nm and 237 nm are observed. These bands are attributed to charge transfer bands (CTBs) arising from transitions between the oxygen 2p orbitals and the 4f levels of Eu^{3+} ions ($O^{2-} \rightarrow Eu^{3+}$) [44,45]. Such CTBs, especially in the deep UV region, have been well-documented in various Eu^{3+}-doped oxide hosts and are indicative of potential host-to-activator energy transfer processes, which can enhance overall emission efficiency.

Upon excitation at 392 nm, the emission spectrum of KSYBO:0.01Eu^{3+} exhibits a prominent peak at 617 nm, corresponding to the $^5D_0 \rightarrow {}^7F_2$ electric dipole transition. This hypersensitive transition dominates the emission profile, indicating that Eu^{3+} ions occupy non-centrosymmetric sites in the host lattice. In contrast, the weaker emission lines observed in the 570–585 nm region are ascribed to the $^5D_0 \rightarrow$

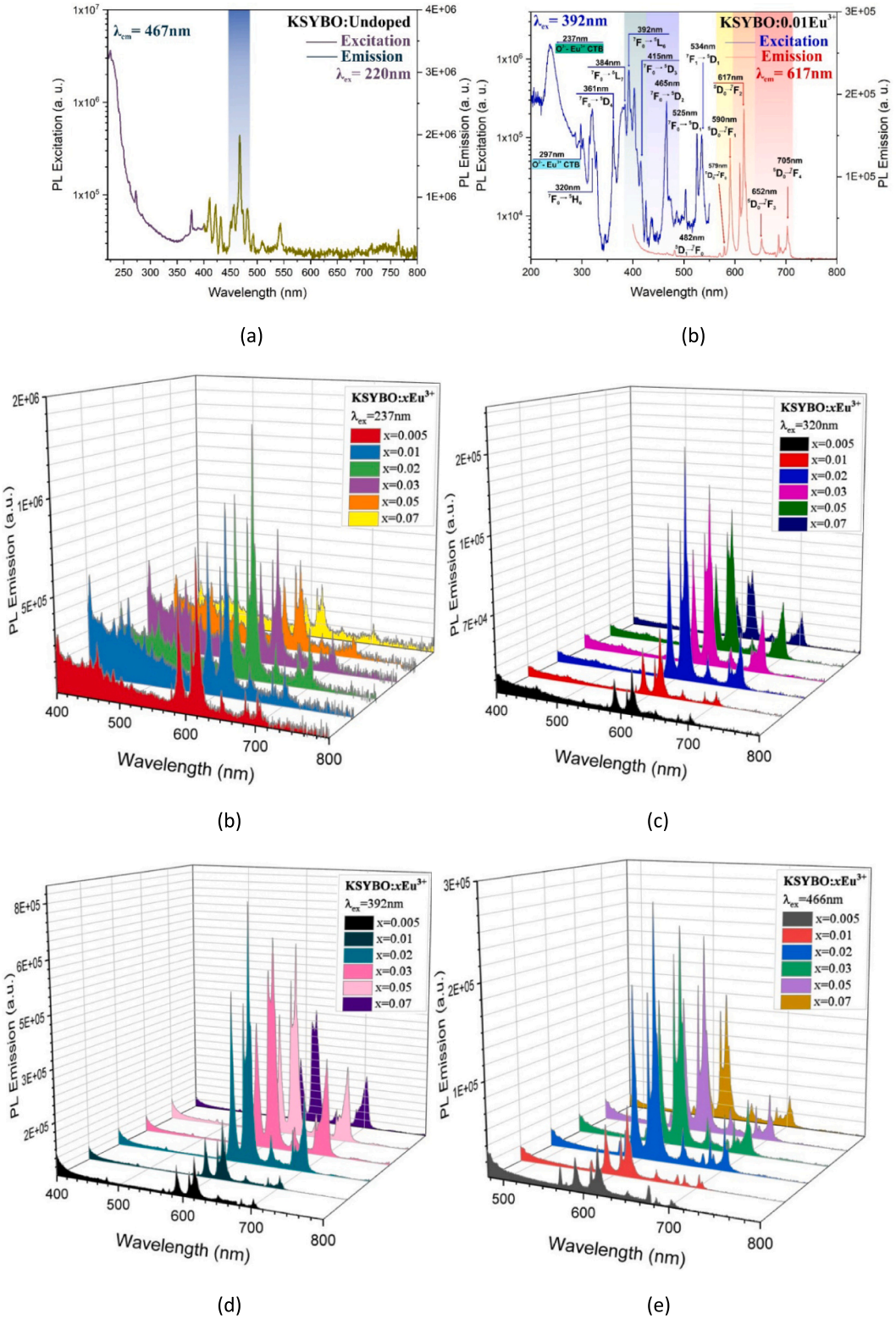

Fig. 5. (a) PL excitation (λ_{em} = 617 nm) and emission (λ_{ex} = 392 nm) spectra of undoped KSYBO host. (b) Combined PL excitation (λ_{em} = 617 nm) and emission (λ_{ex} = 392 nm) spectra of KSYBO:0.01Eu^{3+}. PL emission spectra of KSYBO:xEu^{3+} (x = 0.005–0.07) phosphors under different excitation wavelengths: (c) 237 nm, (d) 320 nm, (e) 392 nm, and (f) 466 nm. Each spectrum highlights the characteristic $^5D_o \rightarrow {}^7F_J$ transitions of Eu^{3+}. (g) Schematic representation of the excitation and emission processes in Eu^{3+}-activated KSYBO: (left) configuration coordinate diagram illustrating excitation via CTB and $^5L_6$ state followed by relaxation to ^5D_o; (right) energy level diagram of Eu^{3+} showing key excitation wavelengths and corresponding radiative transitions.

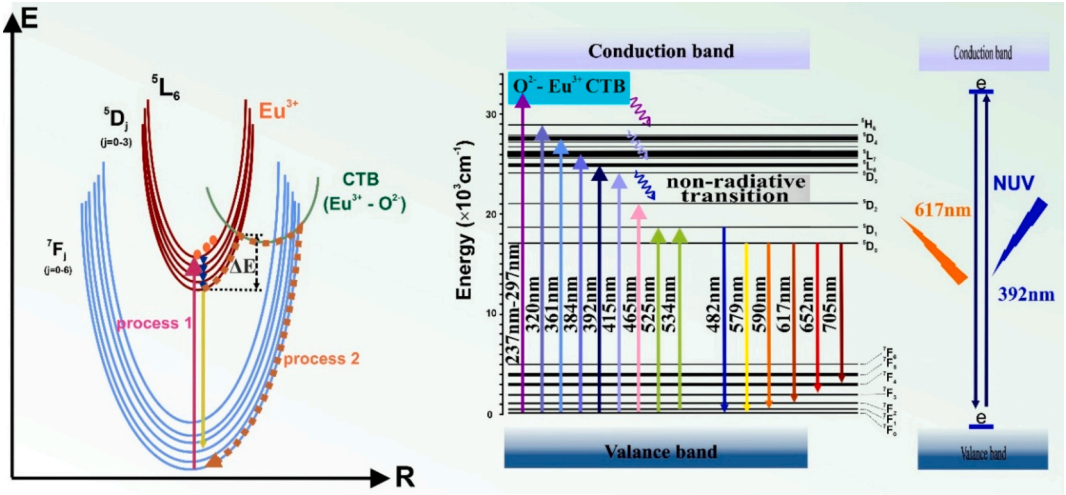

(f)

Fig. 5. (*continued*).

$^7F_0$ and $^5D_0 \rightarrow {}^7F_1$ transitions, which are typically allowed under magnetic dipole or symmetry-perturbed conditions. These relative intensities further support the asymmetric coordination environment around Eu^{3+} in the KSYBO matrix. This behavior is consistent with previous studies that highlighted the relationship between site symmetry and electric/magnetic dipole transition intensities in Eu^{3+}-doped materials [24,46]. Furthermore, the relative intensities of the emission lines offer valuable insight into the crystal field environment surrounding the Eu^{3+} ions. The presence of weaker emission lines at 579, 652, and 705 nm corresponds to transitions to the $^7F_0$, $^7F_3$, and $^7F_4$ levels, respectively, and further supports the multiplet nature of the Eu^{3+} emission spectrum in this host. Notably, the slight splitting observed in the 579 nm region indicates that Eu^{3+} ions may occupy at least two distinct crystallographic sites with different local field environments. Such site-dependent splitting of the $^7F_0$ level has been previously observed in Eu^{3+}-doped glasses and crystals [47,48], supporting the presence of multiple local environments. Although the $^5D_0 \rightarrow {}^7F_4$ transition (705 nm) is typically parity-forbidden and weak, its visible manifestation here suggests a moderate degree of local asymmetry around Eu^{3+} ions, possibly influenced by the structural environment of the KSYBO lattice.

In conclusion, the KSYBO:0.01Eu^{3+} phosphor demonstrates efficient absorption in the near-UV region and strong red emission centered at 617 nm, rendering it a promising candidate for photonic and solid-state lighting applications.

To further explore the excitation-wavelength-dependent photoluminescence behavior of Eu^{3+} in the KSYBO host lattice, PL emission spectra were recorded for various Eu^{3+} concentrations (x = 0.005–0.07) under four distinct excitation wavelengths: 237, 320, 392, and 466 nm, as shown in Fig. 5(c–f). All spectra exhibit the characteristic emission transitions from the $^5D_0$ excited state to the ^7F_J (J = 0–4) ground multiplets of Eu^{3+}, with the most prominent peak consistently located at ~617 nm ($^5D_0 \rightarrow {}^7F_2$), confirming the red-emitting nature of the phosphor.

Under deep-UV excitation band at 237 nm [Fig. 5a], which corresponds to the charge transfer band (CTB) involving $O^{2-} \rightarrow Eu^{3+}$ transitions, an enhanced emission intensity is observed, particularly for x = 0.02. This suggests an efficient host-to-activator energy transfer, leveraging the broad CTB absorption profile. However, at higher Eu^{3+} concentrations ($x > 0.03$), a decline in intensity is noted, indicating the onset of concentration quenching due to non-radiative energy migration among Eu^{3+} ions.

Excitation at 320 nm [Fig. 5d], which likely involves high-energy 4f–4f transitions or residual CTB tail absorption, results in relatively weaker emissions. Nevertheless, the emission patterns remain consistent with those obtained at 237 nm [Fig. 5(c)], supporting the robustness of the radiative transitions from Eu^{3+} centers across various excitation conditions.

The excitation at 392 nm [Fig. 5e] corresponds to the $^7F_0 \rightarrow {}^5L_6$ transition, known for its strong oscillator strength in non-centrosymmetric environments. Here, KSYBO:0.02Eu^{3+} again exhibits the most intense emission, confirming the optimal activator concentration. Notably, the hypersensitive $^5D_0 \rightarrow {}^7F_2$ transition dominates the spectra, further validating the asymmetrical nature of Eu^{3+} coordination in the host lattice.

At 466 nm excitation [Fig. 5(f)], targeting the $^7F_0 \rightarrow {}^5D_2$ transition, the emission intensity is significantly lower compared to 392 nm excitation, consistent with literature reports where higher excitation efficiency is typically achieved near the $^5L_6$ absorption band. The maintained spectral profile across all excitation conditions confirms the chemical stability and spectral fidelity of Eu^{3+} in KSYBO.

To provide a comprehensive understanding of the excitation–emission dynamics observed in KSYBO:Eu^{3+} phosphors, a schematic representation is given in Fig. 5(g). The diagram integrates the major excitation transitions, including both the charge transfer band (CTB) and discrete 4f–4f transitions, with corresponding multiplet emissions from the $^5D_0$ excited level. These visualizations support the experimental observations detailed in Fig. 5d, confirming that Eu^{3+} ions in KSYBO can be efficiently excited across a broad spectral window and that the radiative transitions are strongly modulated by local crystal field symmetry.

These observations demonstrate that the PL emission of KSYBO:Eu^{3+} phosphors can be effectively tuned by altering the excitation wavelength, with 392 nm offering the most intense and stable luminescence. The comparative analysis also reinforces 0.02 Eu^{3+} as the optimal dopant concentration for achieving maximum emission efficiency without significant quenching effects. These results are in agreement with prior studies on Eu^{3+}-activated red phosphors [24], where similar excitation-dependent emission behaviors were reported.

A notable increase in both the 617 nm and 590 nm emission intensities is observed as Eu^{3+} concentration increases from 0.005 to 0.02, indicating enhanced energy absorption and more efficient radiative transitions compared to the weaker emissions at lower doping levels. The emission at 617 nm, corresponding to the electric dipole $^5D_0 \rightarrow {}^7F_2$ transition, exhibits higher sensitivity to the asymmetry of the local site, and its intensity dominates over the magnetic dipole $^5D_0 \rightarrow {}^7F_1$ transition

at 590 nm across all compositions. This asymmetry is further corroborated by the R/O ratio trend, which shows a peak at x = 0.07, suggesting a maximal distortion or lowest symmetry environment around Eu^{3+} ions at this doping level, consistent with previous reports on site-dependent Eu^{3+} emission in perovskite-type hosts [49,50]. After reaching an optimal concentration (2 wt%), both emission bands begin to quench slightly, likely due to concentration quenching mechanisms such as enhanced non-radiative cross-relaxation or energy migration among adjacent Eu^{3+} ions as shown in Fig. 6. The steady increase of the R/O ratio at higher concentrations, even as emission intensity slightly decreases, indicates that the local field asymmetry continues to evolve, possibly due to lattice strain or clustering effects. The observed trend in the R/O ratio aligns well with the variation in emission intensities, providing additional confirmation that changes in the local symmetry around Eu^{3+} ions significantly influence the optical performance of the phosphors. These findings confirm that 392 nm excitation is highly effective for sensitizing Eu^{3+} emission in this system and that both site symmetry and concentration play vital roles in tuning the photoluminescence performance.

To better understand the concentration quenching behavior observed at Eu^{3+} doping levels above 2 wt%, the critical distance (R_c) between neighbouring Eu^{3+} ions was estimated using Blasse's empirical approach. This distance provides insight into the predominant energy transfer mechanism—whether it is exchange-driven or governed by multipolar interactions.

The critical distance can be calculated by the following expression [51,52]:

$$R_c = 2\left(\frac{3V}{4\pi N X_c}\right)^{1/3} \quad (2)$$

where V is the unit cell volume (2305.58 $Å^3$), N is the number of available cation sites per unit cell ($N = 6$), and X_c is the critical concentration of Eu^{3+} (2 wt%).

Substituting the values yields a critical distance of approximately 30.4 Å, which is significantly greater than the threshold value of 5 Å. This large distance rules out exchange interaction as a feasible quenching mechanism and strongly suggests that concentration quenching in the KSYBO:Eu^{3+} system occurs via long-range electric multipole interactions, consistent with the theoretical framework commonly applied in rare-earth-doped borate systems [53]. Such findings are consistent with previous studies on Eu^{3+}-doped hosts where similar distances led to dominant dipole–dipole interactions, aligning with the trend observed in the evolution of the PL intensity and red-to-orange (R/O) emission ratio [54]. As Eu^{3+} ions come into closer proximity at higher concentrations, non-radiative multipolar interactions become more prominent, facilitating energy migration and eventual quenching.

To investigate the origin of concentration quenching observed in Eu^{3+}-doped KSYBO phosphors, the approach proposed by Van Uitert was utilized [55]. This framework establishes a relationship between photoluminescence intensity (I) and dopant concentration (x) using a logarithmic formulation:

$$Log\left(\frac{I}{x}\right) = -\frac{\theta}{3}log(X) + A \quad (3)$$

where θ represents the interaction parameter, indicative of the dominant multipolar interaction, and A is a constant. In this formalism, values of θ = 6, 8, and 10 correspond to dipole–dipole, dipole–quadrupole, and quadrupole–quadrupole interactions, respectively.

In our system, the linear fit of the experimental data yielded a slope of −1.83 as shown in Fig. 6b. Substituting this value into Eq. (3) $\theta \approx 5.49$, closely matching the theoretical value for dipole–dipole interaction ($\theta = 6$). This agreement indicates that non-radiative energy transfer between Eu^{3+} ions at higher doping concentrations is predominantly governed by dipole–dipole interactions. This conclusion is further supported by the critical distance (R_c) analysis, collectively demonstrating that reduced interionic distances promote non-radiative energy transfer. Thus, the observed concentration quenching arises from enhanced dipole–dipole coupling at elevated Eu^{3+} densities.

3.6. *Influence of monovalent co-dopants on photoluminescence and decay behavior*

Fig. 7a and b show the normalized PL emission spectra of KSYBO:0.02Eu^{3+} phosphors co-doped with varying concentrations of Li^+ (a) and Na^+ (b) under 392 nm excitation. All spectra were normalized with respect to the $^5D_0 \rightarrow {}^7F_2$ transition at ~612 nm to emphasize relative variations in the $^5D_0 \rightarrow {}^7F_4$ emission. A clear compositional dependence is observed, especially for the 705 nm band ($^5D_0 \rightarrow {}^7F_4$), which increases significantly with Li^+ co-doping. In contrast, Na^+ co-doping yields only a modest rise in the same transition, whereas the y = 0 sample represents Eu^{3+}-only without alkali ion addition. These results highlight the influence of monovalent co-dopants on the asymmetry of the local crystal field surrounding Eu^{3+} ions. A distinct enhancement is observed in both the primary red-emitting transition at 617 nm ($^5D_0 \rightarrow {}^7F_2$) and the lower-energy transition at 705 nm ($^5D_0 \rightarrow$

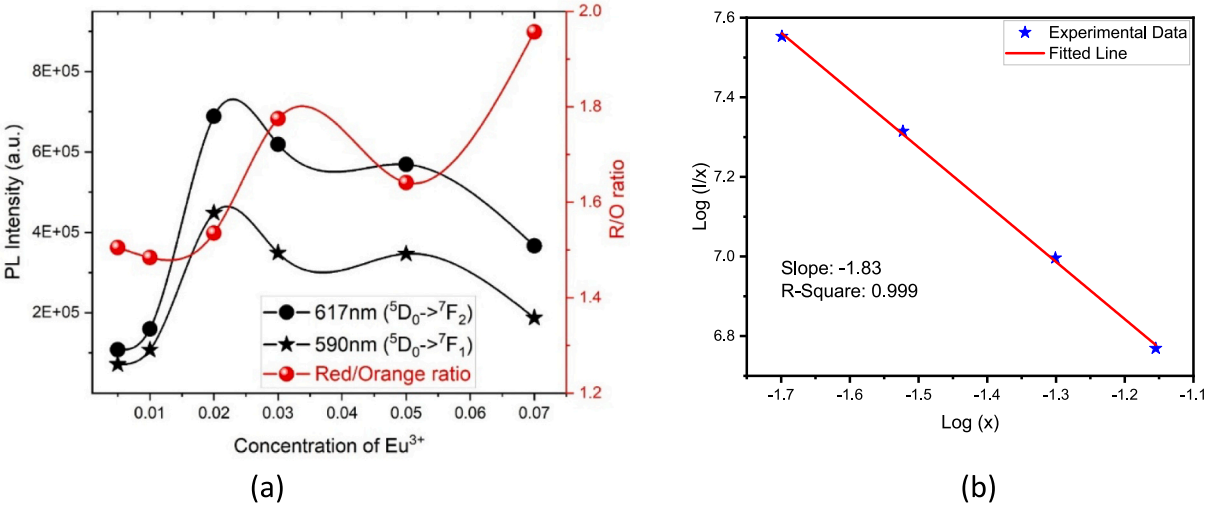

Fig. 6. Integrated PL intensities of the electric dipole transition ($^5D_0 \rightarrow {}^7F_2$, 617 nm) and magnetic dipole transition ($^5D_0 \rightarrow {}^7F_1$, 590 nm) as a function of Eu^{3+} concentration under 392 nm excitation.

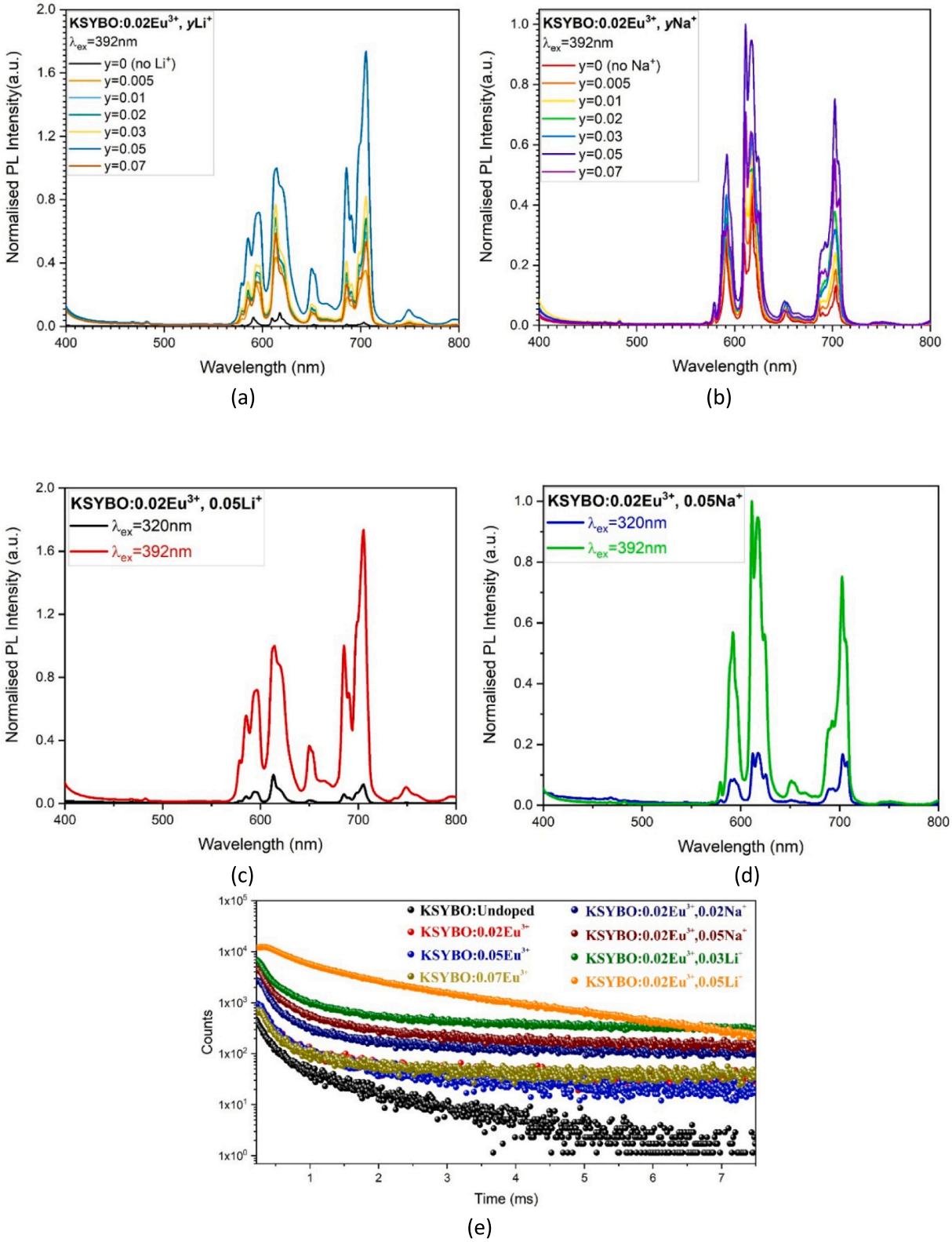

Fig. 7. 3D PL emission spectra of KSYBO:0.02Eu^{3+} co-doped with varying concentrations of Li^+ (a) and Na^+ (b) under 392 nm excitation. The label y = 0 (no Li^+ or Na^+) corresponds to a sample exclusively with Eu^{3+}, without any alkali ion co-doping. All spectra were recorded under identical experimental conditions, with the Eu^{3+} concentration fixed at 2 wt%. PL emission spectra of (c) KSYBO:0.02Eu^{3+}, 0.05Li^+ and (d) 0.05Na^+ under 320 nm and 392 nm excitation, illustrating the excitation-dependent variation in $^5D_0 \rightarrow {}^7F_4$ transition intensity. (e) Time-resolved decay curves for selected KSYBO:Eu^{3+} and Eu^{3+}/M^+ (M = Li^+, Na^+) compositions illustrating the impact of co-doping on luminescence lifetimes.

$^7F_4$), albeit to very different extents depending on the dopant ion. The $^5D_0 \rightarrow {}^7F_J$ (J = 0–4) transitions originate from the same excited level but terminate at different Stark sublevels of the ^7F ground multiplet manifold, with $^7F_4$ corresponding to the lowest energy (longest wavelength) emission typically observed in Eu^{3+} spectra. At 617 nm, Li^+ co-doping yields a marginal increase (~1.02-fold), while Na^+ leads to a more pronounced enhancement (~1.88-fold), indicating moderate modulation of the hypersensitive $^5D_0 \rightarrow {}^7F_2$ transition. However, the emission at 705 nm displays an exceptionally anomalous trend: Li^+ co-doping boosts this transition by an astounding ~58-fold, whereas Na^+ co-doping results in a more modest ~5-fold enhancement.

Such a disproportionate amplification of the $^5D_0 \rightarrow {}^7F_4$ emission upon Li^+ incorporation points to a strong influence of local crystal field distortion, likely originating from the smaller ionic radius of Li^+. This aligns with the findings of Ling-Hu et al. [56], who reported anomalously intense $^7F_4$ transitions in systems where structural distortion breaks the parity-selection rules, enabling stronger electric dipole transitions.

To better illustrate the dependence of the $^5D_0 \rightarrow {}^7F_4$ emission intensity on excitation wavelength, the emission spectra of KSYBO:0.02Eu^{3+}, 0.05Li^+ and KSYBO:0.02Eu^{3+}, 0.05Na^+ were normalized with respect to the $^5D_0 \rightarrow {}^7F_2$ transition at ~612 nm (Figs. 7 c-d). As can be seen, the relative intensity of the $^5D_0 \rightarrow {}^7F_4$ transition (centered around ~700 nm) varies significantly between 320 nm and 392 nm excitation, indicating the influence of the excitation pathway on the local environment and symmetry of Eu^{3+} ions. This behavior confirms the excitation-dependent asymmetry around Eu^{3+} centers.

Li^+, with its higher field perturbation capacity, may induce a highly asymmetric coordination environment around Eu^{3+}, intensifying transitions that are normally weak or parity-forbidden. This selective enhancement suggests that the $^7F_4$ band, although typically overshadowed by $^7F_2$ emissions, can become dominant under specific structural distortions—offering a powerful tool for tuning spectral output and chromaticity in photonic applications.

To further elucidate the influence of monovalent co-doping on Eu^{3+} photoluminescence dynamics, time-resolved decay profiles were recorded for selected compositions, as shown in Fig. 7e. The undoped KSYBO host exhibits a relatively fast and weak decay, indicative of negligible radiative processes. Upon introducing 0.02 Eu^{3+}, a pronounced elongation in decay lifetime is observed (τ_{avg} = 0.992 ms), confirming the activation of Eu^{3+}-related radiative pathways. Interestingly, further increase in Eu^{3+} content results in a reduced τ_{avg}, reaching 0.775 ms at 0.07, which aligns well with the concentration quenching trend previously discussed.

A notable enhancement in lifetime is evident with Li^+ and Na^+ co-doping. In particular, Li^+ addition (y = 0.03 and 0.05) markedly extends the average lifetime to 1.441 ms—surpassing all other compositions. This suggests that Li^+ incorporation not only suppresses non-radiative losses but also stabilizes Eu^{3+} excited states, possibly via local crystal field modulation or charge compensation effects that reduce lattice defects. The prolonged decay may also be related to the enhanced $^5D_0 \rightarrow {}^7F_4$ transition intensity, as previously discussed in the anomalous emission section. This observation is further substantiated by the lifetime data, as summarized in Table 3, where both 0.03Li^+ and 0.05Li^+ co-doped samples show the longest τ_{avg} values (~1.441 ms). Such prolongation in decay behavior suggests that the anomalous enhancement of the $^5D_0 \rightarrow {}^7F_4$ emission is not merely a spectral artifact but is temporally supported, implying stronger radiative transition probabilities. Similarly, Na^+ co-doping at 2 wt% ratio significantly prolongs the Eu^{3+} lifetime to 1.870 ms, surpassing even Li^+ in some cases. This extended lifetime, coupled with the moderate enhancement in $^5D_0 \rightarrow {}^7F_4$ emission intensity, suggests that Na^+ also modulates the local crystal field and electronic environment around Eu^{3+} ions, albeit through different structural mechanisms than Li^+. The distinct lifetimes and emission responses highlight the differentiated roles of Li^+ and Na^+ co-dopants in tailoring the optical performance of KSYBO:Eu^{3+} phosphors. Although a detailed Judd–Ofelt analysis will follow in a subsequent section, this temporal evidence strengthens the argument that Li^+ co-doping significantly alters the local field symmetry around Eu^{3+} ions, promoting the intensity of hypersensitive transitions.

Table 3
Average luminescence lifetimes (τ_{avg}) of Eu^{3+}-activated KSYBO phosphors with and without monovalent ion co-doping.

		Time(μs)	Rel.%	τ_{avg}(ms)	χ^2
KSYBO:Undoped	τ_1	11.45	31.33	1.129	1.166
	τ_2	34.19	24.14		
	τ_3	1270.48	44.53		
KSYBO:0.02Eu^{3+}	τ_1	10.18	34.73		
	τ_2	437.20	31.22	0.992	1.062
	τ_3	1600.80	34.05		
KSYBO:0.05Eu^{3+}	τ_1	10.89	35.33		
	τ_2	459.60	27.33	0.959	1.118
	τ_3	1416.80	37.34		
KSYBO: 0.07Eu^{3+}	τ_1	12.67	48.48	0.775	1.053
	τ_2	847.20	51.52		
KSYBO:0.02Eu^{3+},0.02Na^+	τ_1	11.74	37.69		
	τ_2	527.20	31.13	1.870	1.197
	τ_3	3434.80	31.18		
KSYBO:0.02Eu^{3+},0.05Na^+	τ_1	10.93	31.48		
	τ_2	414.50	32.96	1.142	1.178
	τ_3	1915.40	35.56		
KSYBO:0.02Eu^{3+},0.03Li^+	τ_1	11.05	25.14		
	τ_2	437.02	36.50	1.441	1.175
	τ_3	2490.08	38.36		
KSYBO:0.02Eu^{3+},0.05Li^+	τ_1	427.83	29.90	1.441	1.657
	τ_2	1873.75	70.10		

In contrast, Na^+ co-doping also increases τ_{avg} values (1.142 and 1.870 ms), but not to the same extent as Li^+. This difference may be attributed to the ionic radius mismatch and distinct effects of Na^+ on the crystal symmetry and site occupancy. Collectively, these results corroborate the steady-state PL findings, affirming that monovalent ion co-doping—particularly with Li^+—is an effective strategy to prolong luminescence lifetimes and improve optical performance in Eu^{3+}-activated KSYBO phosphors.

3.7. Temperature-dependent photoluminescence behavior of KSYBO:Eu^{3+} and Li^+ co-doped systems

To evaluate the thermal stability and emission dynamics of Eu^{3+}-doped KSYBO phosphors under elevated temperatures, temperature-dependent photoluminescence (TDPL) spectra were recorded for both KSYBO:0.02Eu^{3+} and Li^+ co-doped KSYBO:0.02Eu^{3+},0.05Li^+ compositions (Fig. 8a–b). The measurements span the 300–550 K range under 392 nm excitation, revealing key insights into emission retention and quenching mechanisms.

As shown in Fig. 8a, the KSYBO:0.02Eu^{3+} sample exhibits typical thermal quenching behavior, where PL intensity progressively decreases with rising temperature. This decline is attributed to enhanced phonon-assisted non-radiative relaxation pathways that compete with radiative $^5D_0 \rightarrow {}^7F_j$ transitions of Eu^{3+} ions. At 550 K, the PL intensity drops to less than 20 % of its initial value at room temperature, indicating moderate thermal stability.

In contrast, the Li^+ co-doped counterpart (Fig. 8b) maintains significantly higher PL intensity across the same temperature range. Even at 550 K, over 40 % of the room-temperature emission is retained. This improvement suggests that Li^+ incorporation enhances the rigidity and local field symmetry of the host lattice, thereby suppressing non-radiative losses. While Li^+ ions are often described as mobile or "restless" in disordered systems such as glasses or ionic conductors, their incorporation into a crystalline borate host like KSYBO leads to localized lattice strain rather than enhanced ionic conductivity. The aliovalent substitution and small ionic radius (0.76 Å) of Li^+ allow it to occupy interstitial or off-centered substitutional positions, introducing short-

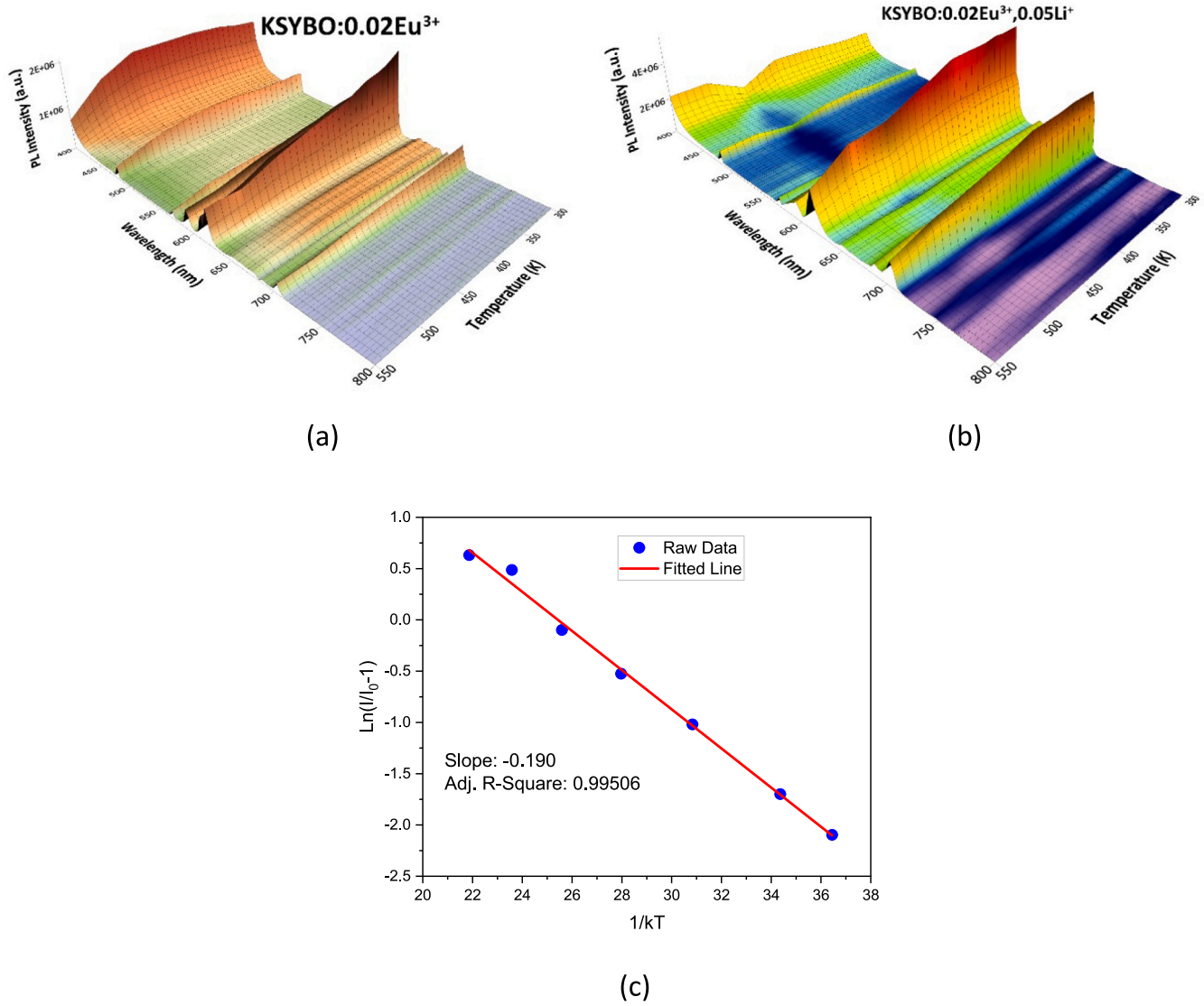

Fig. 8. Temperature-dependent photoluminescence (PL) spectra of (a) KSYBO:0.02Eu^{3+} and (b) KSYBO:0.02Eu^{3+},0.05Li^{+} phosphors in the 300–500 K range under 395 nm excitation. (c) Arrhenius plot derived from the thermal quenching behavior of KSYBO:0.02Eu^{3+} phosphor.

range asymmetry and strain fields that increase the effective local rigidity. This local distortion modifies the phonon spectrum and redistributes vibrational modes in such a way that non-radiative multiphonon relaxation is suppressed.

These effects, corroborated by the enhanced activation energy and PL lifetime, reflect a structural stiffening around Eu^{3+} sites rather than global lattice stiffening, consistent with the observed photophysical trends. Furthermore, the PL intensity at room temperature is notably higher in the Li^{+}-doped sample, consistent with earlier steady-state and lifetime results.

The emission profiles remain centered around the characteristic 617 nm transition ($^5D_0 \rightarrow {}^7F_2$), with no significant spectral shift observed upon heating, reaffirming the chemical stability and site occupation of Eu^{3+} ions in the trigonal borate matrix. This thermal resilience highlights the potential of Li^{+} co-doping in extending the operational temperature range of red-emitting phosphors.

To quantitatively assess the thermal quenching resistance, the activation energy (E_a) of thermal quenching was calculated using the Arrhenius equation model for the KSYBO:0.02Eu^{3+}:

$$ln\left(\frac{I_o}{I}-1\right)=\frac{E_a}{kT}+C \quad (4)$$

where I_0 and I denote the PL intensities at room temperature and elevated temperatures, respectively, k is Boltzmann's constant, and T is the absolute temperature. The linear fit of $ln[(I_0/I-1)]$ *vs* $1/kT$ is shown in Fig. 8c. The slope of the fitted line corresponds to the activation energy E_a, calculated as 0.19087 eV. This Ea value provides a quantitative benchmark for assessing the efficiency of Li^{+} co-doping in enhancing thermal stability. The significantly better PL retention in the Li^{+} co-doped sample (Fig. 8b) suggests that the co-doping effectively increases the energy barrier for non-radiative relaxation, although a separate E_a analysis for this sample is needed for full comparison. The high correlation coefficient ($R^2 = 0.99589$) validates the accuracy of the fitting and supports the thermal stability trend observed in the TDPL spectra. To further contextualize this result, Table 4 compares the calculated E_a value of KSYBO:Eu^{3+}, Li^{+} with other reported Eu^{3+}-doped red-emitting phosphors. The activation energy of 0.190 eV observed in this study is among the highest values, exceeding those reported for compounds such as $Ca_3B_2O_6$:Eu^{3+} (0.179 eV) [57] and

Table 4
Comparison of activation energies (E_a) of KSYBO: Eu^{3+}, Li^+ with other reported Eu^{3+}-doped red-emitting phosphors.

Compound	E_a (activation Energy)	Ref.
KSYBO:Eu, Li^+	0.190 eV	This work
$Ca_3B_2O_6$: 0.010Eu^{3+}	0.179 eV	[57]
$Na_2Y_2B_2O_7$:0.35Eu^{3+}	0.160 eV	[58]
$K_7SrY_2B_{15}O_{30}$: Eu^{3+}	0.172 eV	[61]
$Gd_7O_6(BO_3)$ $(PO_4)_2$: 1.4Eu^{3+}	0.177 eV	[62]
$Ca_3Eu_2B_4O_{12}$	0.179 eV	[63]
$Na_2Gd_2B_2O_7$:0.35Eu^{3+}	0.148 eV	[64]
KYBO:0.05Eu^{3+},0.01Li^+	0.138 eV	[54]

$Na_2Y_2B_2O_7$:0.35Eu^{3+} (0.160 eV) [58]. This comparison reinforces the superior thermal stability of the KSYBO host matrix.

Such high activation energy values are advantageous for thermally robust phosphors in high-power LED applications, highlighting KSYBO: Eu^{3+},Li^+ as a promising candidate for practical solid-state lighting systems.

Similar methodologies and activation energy values have been reported for thermally stable Eu^{3+}-based red phosphors used in high-power LED applications, indicating that the current KSYBO host is a promising candidate for practical solid-state lighting systems.

While the activation energy (E_a = 0.190 eV) determined for Li^+ co-doped KSYBO:Eu^{3+} phosphors indicates high thermal stability, a more nuanced mechanistic explanation is warranted. In many rare-earth flavoured phosphor systems, thermal quenching originates from multi-phonon relaxation: excited electrons are thermally promoted to a crossing point between excited and ground state potential curves, facilitating non-radiative decay—an effect well described by the configurational-coordinate model [59].

Specifically, in Li^+-doped borate hosts, co-doping has been shown to reduce phonon density and shift the crossover point, thereby raising the quenching barrier. For example, a recent study on $SmCa_4O(BO_3)_3$:Eu^{3+}, Li^+ demonstrated that Li^+ co-doping enhances crystallinity and reduces non-radiative losses via modulation of phonon modes [5]. Similarly, research on Eu^{3+} doped borates has found that Li^+ and Na^+ co-dopants significantly enhance luminescent efficiency and thermal stability due to suppression of phonon-mediated quenching [54,60]. Therefore, the improved thermal resilience in KSYBO: Eu^{3+}, Li^+ phosphors likely stems from a combined mechanism: (1) increased lattice rigidity reducing phonon coupling; (2) realignment of the potential energy curves in configurational-coordinate space; and (3) suppression of multiphonon relaxation despite the relatively high phonon energy (~1325–1400 cm^{-1}) of BO_3/BO_4 groups, which are indeed considered high compared to fluorides or tungstates – may arise from the compact and rigid borate framework, particularly the vibrational decoupling within the $[B_5O_{10}]^{5-}$ clusters. This tripartite mechanism creates a powerful synergy that effectively suppresses non-radiative deactivation pathways in Eu^{3+} emission centers.

3.8. *Judd–Ofelt analysis for KSYBO:0.02Eu^{3+}, 0.05Li^+ phosphors*

The Judd–Ofelt (J–O) intensity parameters Ω_λ (λ = 2,4,6) for the KSYBO:0.02Eu^{3+},0.05Li^+ phosphors were determined using the classical Judd-Ofelt formalism [65,66], which models the intensity of electric dipole transitions in rare-earth ions embedded in crystalline hosts.

The calculation utilizes the following equation:

$$A_{ED} = \frac{64\pi^4 e^2 n(n^2+2)^2}{3h(2J+1)9c\lambda^3}.\Omega_\lambda.\left|\left\langle 5D_0\right\|U^{(\lambda)}\left\|7F_J\right\rangle\right|^2 \quad (5)$$

where, in Eq. 5:

A_{ED} is the spontaneous emission probability for electric dipole transitions.

Ω_λ (λ = 2,4,6) are the Judd–Ofelt intensity parameters.

$\left\langle 5D_0\right\|U^{(\lambda)}\left\|7F_J\right\rangle$ are the doubly reduced matrix elements taken from Carnall et al. [67].

n is the refractive index of the host (assumed as 1.46) [22,68].

J is the total angular momentum of the initial state (here, J=0).

λ is the wavelength (in cm) of the transition.

To extract Ω_λ values, the integrated emission intensities of the $^5D_0 \rightarrow {}^7F_1$, $^7F_2$, and $^7F_4$ transitions were used in combination with the magnetic dipole transition ($^5D_0 \rightarrow {}^7F_1$) as a reference. This approach ensures normalization and consistency in the evaluation of electric dipole strengths. The matrix-independent constant ($S_{md} = 7.83 \times 10^{-42}$ cm^2) was used as a scaling factor in the transition intensity comparison. All spectral data were corrected for instrumental response and calibrated against a standard reference.

To proceed with the Judd–Ofelt analysis, the integrated emission intensities of the $^5D_0 \rightarrow {}^7F_j$ (J = 1, 2, 4) transitions were quantitatively extracted from the photoluminescence spectra, following instrumental correction. These values, summarized in Table 5, served as the primary input for calculating the intensity parameters Ω_2, Ω_4, and Ω_6. The $^5D_0 \rightarrow {}^7F_1$ magnetic dipole transition was used as an internal reference to normalize the electric dipole transitions.

Based on the integrated emission intensities of the $^5D_0 \rightarrow {}^7F_j$ (J = 1, 2, 4) transitions (Table 5), J–O intensity parameters were calculated to be $\Omega_2 = 2.08 \times 10^{-20}$ cm^2, $\Omega_4 = 3.95 \times 10^{-20}$ cm^2; $\Omega_6 = 5.42 \times 10^{-20}$ cm^2, indicating significant structural distortion in the local environment of Eu^{3+} ions, similar to that observed in other non-centrosymmetric rare-earth-doped hosts. The unusually high Ω_6 value obtained (5.42×10^{-20} cm^2) suggests a pronounced contribution from the $^5D_0 \rightarrow {}^7F_4$ transition. This trend aligns with recent findings in Eu^{3+}-activated alkali borate systems, such as those reported by Luewarasirikul and Kaewkhao [69], where the $^5D_0 \rightarrow {}^7F_4$ emission intensity was significantly enhanced due to increased local asymmetry and lattice distortion in borate glass matrices. These factors are known to contribute to an elevated Ω_6 value, even in systems that typically exhibit centrosymmetric behavior. The observed Ω_2 value suggests significant asymmetry at the Eu^{3+} sites, consistent with local crystal field distortion induced by Li^+ co-doping. However, its magnitude remains within the typical range reported for distorted Eu^{3+} environments in borates, and is therefore not interpreted as unusually high in this context. Rather, it reflects the expected crystal field asymmetry due to Li^+ incorporation, consistent with known borate systems [1]. Likewise, the moderately large Ω_4 suggests increased covalency or a more rigid crystal field, often linked to stronger host-ligand interactions.

Furthermore, to deepen the interpretation of the local symmetry effects, the ratio of Ω_2 to Ω_6 (Ω_2/Ω_6) was evaluated. This ratio serves as a sensitive indicator of the relative contributions of hypersensitive electric dipole transitions versus symmetry-induced forbidden transitions. In the present study, the Ω_2/Ω_6 value was calculated to be significantly less than unity, underscoring the dominant role of the $^5D_0 \rightarrow {}^7F_4$ transition over the $^5D_0 \rightarrow {}^7F_2$ line. Such a trend is a clear spectroscopic signature of pronounced structural distortion and symmetry breaking around the Eu^{3+} ion, induced by Li^+ co-doping. This finding is in strong agreement with the anomalous emission enhancement observed and supports the conclusion that Li^+ incorporation generates a highly perturbed crystal

Table 5
Integrated emission peak areas of the $^5D_0 \rightarrow {}^7F_J$ transitions of the investigated sample. The measurements were obtained from the emission spectra, and the intensities are given in arbitrary units.

Transition	Wavelength (nm)	Area (KSYBO:0.02Eu^{3+}, 0.05Li^+)	Area (KSYBO:0.02Eu^{3+})
$^5D_0 \rightarrow {}^7F_1$	590	64,353,026	3,567,907
$^5D_0 \rightarrow {}^7F_2$	617	152,818,787	6,446,990
$^5D_0 \rightarrow {}^7F_3$	705	165,879,891	1,934,206

field environment, thereby intensifying parity-forbidden transitions.

Radiative transition rates ($A_{J\to J'}$) for magnetic dipole (MD) and electric dipole (ED) transitions were calculated according to J-O theory using the following expressions (Eq.6 and Eq.7), in line with previous literature [70–75]:

$$A_{J\to J'}^{MD} = \frac{64\pi^4\nu^3}{3h(2J+1)} n^3 S_{MD} \tag{6}$$

$$A_{J\to J'}^{ED} = \frac{64\pi^3\nu^3 e^2}{3h(2J+1)} \frac{n(n^2+2)^2}{9} \Omega_\lambda \left\langle \langle \Psi J \rangle \middle| U^\lambda \middle| \psi' J' \right\rangle^2 \tag{7}$$

Here, ν is the transition wavenumber, h is Planck's constant, and J is the total angular momentum quantum number of the excited state. The parameter n is the refractive index of the host medium. In the case of MD transitions, S_{MD} is the magnetic dipole line strength, a known constant specific to Eu^{3+} $^5D_0 \to {}^7F_1$ transitions. For electric dipole transitions, the squared reduced matrix element $\left\langle \langle \Psi J \rangle \middle| U^\lambda \middle| \psi' J' \right\rangle$ quantifies the electric dipole transition amplitude, and Ω_λ accounts for the angular and symmetry-dependent intensity parameters. The operator $U^{(\lambda)}$ is associated with tensor interactions governing ED transitions [67]. Eqs. (6) and (7) form the theoretical basis for estimating spontaneous emission rates, a critical step in the photophysical interpretation of rare-earth-doped phosphors.

The calculated radiative transition probabilities (A) and branching ratios (β) for the $^5D_0 \to {}^7F_J$ transitions are summarized in Table 6. The branching ratio for each J level is determined using:

$$\beta_{0-J} = \frac{A_{0-J}}{\sum_{J=0,1,2,3,4} A_{0-J}} \tag{8}$$

Here, A_{0-J} represents the radiative transition probability from the $^5D_0$ level to a given ^7F_J level. The branching ratio quantifies the fractional contribution of each individual transition to the overall radiative decay process, thereby providing insight into the emission spectral profile and transition probabilities within the multiplet. In order to verify the theoretical predictions, experimental branching ratios were also determined based on the integrated emission intensities of the $^5D_0 \to {}^7F_J$ transitions. A comparison revealed reasonable agreement between the theoretical and experimental values. Notably, the $^5D_0 \to {}^7F_4$ transition exhibited the highest experimental β value, exceeding the theoretically dominant $^5D_0 \to {}^7F_2$ line. This discrepancy is attributed to the strong local asymmetry induced by Li^+ co-doping, which enhances electric dipole strength and promotes parity-forbidden transitions such as $^5D_0 \to {}^7F_4$. A similar trend has been observed in borate-based hosts such as ZnO–Na_2O–B_2O_3:Eu^{3+}, where enhanced $^5D_0 \to {}^7F_4$ intensity was attributed to local asymmetry and increased Judd–Ofelt Ω_6 values [76].

As shown in Table 6, the $^5D_0 \to {}^7F_2$ transition exhibits the highest branching ratio (41.2 %), indicating that it serves as the dominant radiative decay pathway for the Eu^{3+} ion. The $^5D_0 \to {}^7F_4$ transition also contributes substantially (38.2 %), suggesting a comparable role in the overall emission process. In contrast, the $^5D_0 \to {}^7F_1$ magnetic dipole transition displays a significantly lower branching ratio (20.7 %), indicating a minor contribution to the total photoluminescence output.

Table 6
Radiative transition probabilities and branching ratios for $^5D_0 \to {}^7F_J$ transitions.

Transition	A (s^{-1})	Branching Ratio β (%) (Theoretical)	Branching Ratio β (%) (Experimental)
$^5D_0 \to {}^7F_1$	157.8	20.7	16.8
$^5D_0 \to {}^7F_2$	313.9	41.2	39.9
$^5D_0 \to {}^7F_4$	291.1	38.2	43.3

3.9. Impact of monovalent co-doping on $^5D_0 \to {}^7F_4$ transition and corresponding chromaticity shifts

The role of monovalent ion co-doping on the spectral characteristics of Eu^{3+} emission in KSYBO phosphors was investigated with specific focus on the $^5D_0 \to {}^7F_4$ transition. Although this transition is typically weak due to its parity-forbidden nature, structural distortions induced by alkali ions may relax selection rules, leading to intensity enhancement. The photoluminescence (PL) trends are examined in conjunction with chromaticity coordinates derived from CIE 1931 diagrams (Fig. 9a–c), which offer a cumulative representation of spectral distribution and emission color.

In Fig. 9a, Eu^{3+}-only doped samples are displayed. With increasing Eu^{3+} concentration, the CIE coordinates shift progressively toward deeper red hues, primarily due to enhanced electric dipole $^5D_0 \to {}^7F_2$ transitions. The coordinates remain tightly grouped, indicating minimal contributions from the $^7F_4$ band, which is spectroscopically weak under symmetrical local environments.

Fig. 9b illustrates the effect of Na^+ co-doping. Across all Eu^{3+} levels, chromaticity coordinates show minimal displacement and remain concentrated in a narrow zone, suggesting that Na^+ incorporation does not substantially alter the local crystal field. Although a modest (~5-fold) increase in the $^7F_4$ transition intensity was observed in PL spectra, this is insufficient to cause a perceptible shift in chromaticity. These results support the interpretation that Na^+, while structurally incorporated, introduces only limited asymmetry and functions primarily as a weak field modifier rather than a charge compensator.

Conversely, Fig. 9c demonstrates a broader distribution of chromaticity points in the Li^+ co-doped series. This spread correlates with the anomalously high enhancement (~58-fold) of the $^5D_0 \to {}^7F_4$ emission, suggesting a pronounced local symmetry breaking around Eu^{3+} ions, analogous to trends reported in BaLaGaO$_4$:Eu^{3+} systems [56]. Judd–Ofelt analysis further supports this interpretation with a significantly elevated Ω_6 value, indicating increased electric dipole character. Although CIE coordinates cannot resolve individual transitions, the broadened chromaticity dispersion is consistent with enhanced $^7F_4$ spectral contributions and may reflect energy level splitting within the ^7F_J manifold under asymmetric fields, as proposed by Ling-Hu et al. [56].

To quantitatively evaluate this effect, the color purity and correlated color temperature (CCT) were calculated using chromaticity coordinates derived from emission spectra. The analytical expressions employed are as follows [77]:

$$\textit{Color Purity}\ (\%) = \frac{\sqrt{(x-x_i)^2+(y-y_i)^2}}{\sqrt{(x_d-x_i)^2-(y_d-y_i)^2}} \times 100 \tag{9}$$

where (x, y) are the sample coordinates, $(x_i, y_i) = (0.3127, 0.3290)$ is the standard D65 white point, and (x_d, y_d) corresponds to the dominant wavelength in the red spectral region [78].

$$n = \frac{x-0.3320}{y-0.1858}, \tag{10}$$

$$CCT = -437n^3 + 3601n^2 - 6861n + 5514.31 \tag{11}$$

These equations allow for a quantitative assessment of chromatic saturation and warmth of emission. As summarized in Table 7, the Na^+ co-doped sample exhibits the highest color purity (97.7 %) and the lowest CCT (2253 K), highlighting its deep red chromaticity, which is consistent with earlier reports on Eu^{3+}-activated borate systems such as $K_3Y(BO_2)_6$, where intense red emission and warm CCT values were observed due to host-induced symmetry modulation and efficient energy transfer mechanisms, particularly enhanced by alkali ion co-doping [54]. Li^+ co-doping also enhances color purity (93.4 %) and produces warm white emission (2444 K), aligning with its role in lattice distortion

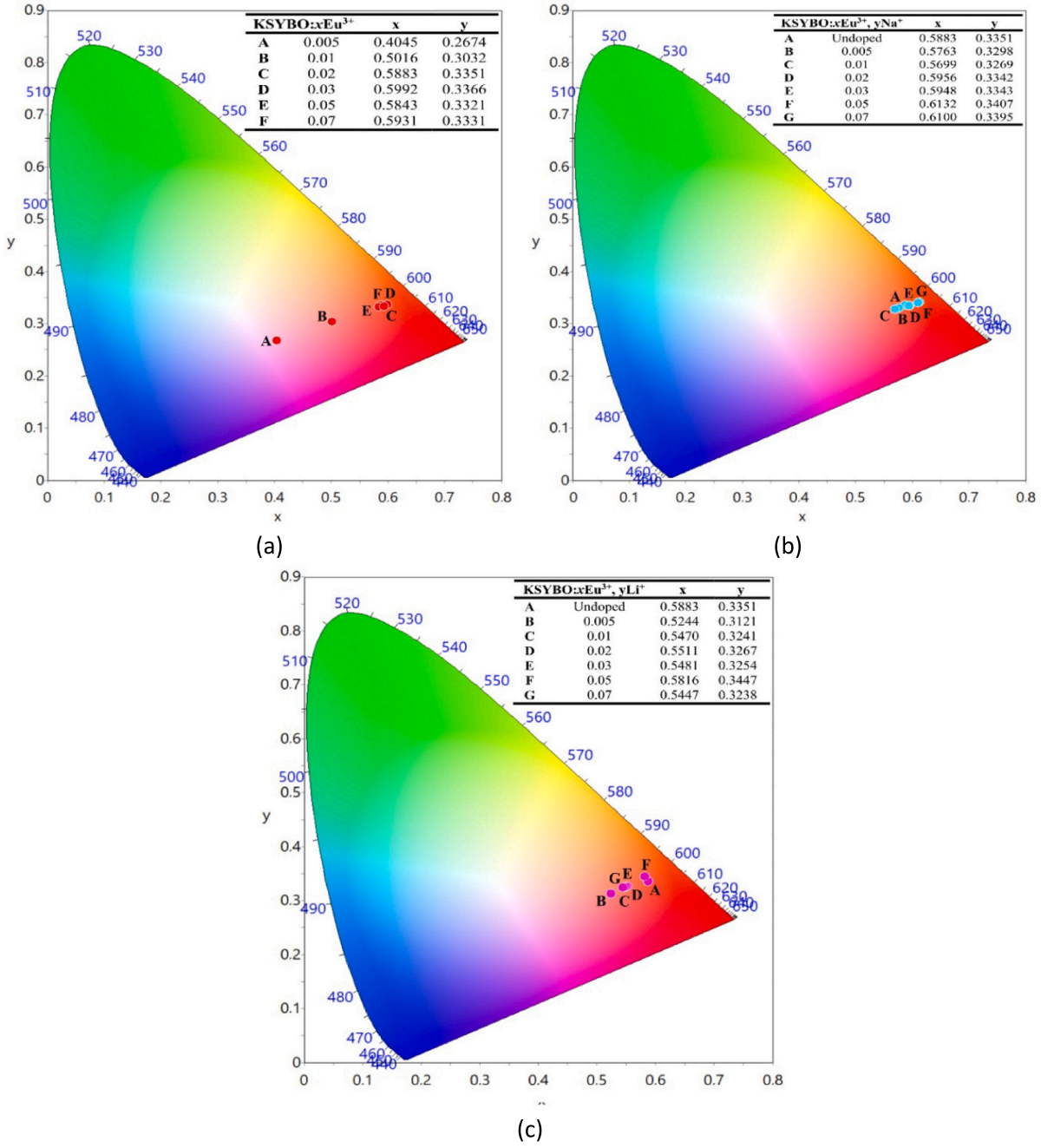

Fig. 9. CIE 1931 chromaticity coordinates of $K_7SrY_2(B_5O_{10})_3:Eu^{3+}$ phosphors with varying Eu^{3+} concentrations and alkali ion co-doping: (a) Eu^{3+}-only doped samples, (b) Na^+ co-doped samples, and (c) Li^+ co-doped samples.

Table 7
CIE Coordinates, Color Purity, and CCT of KSYBO:Eu^{3+} phosphors under 392 nm excitation.

Composition	CIE (x, y)	Color Purity (%)	CCT (K)
KSYBO:0.02Eu^{3+}	(0.5883, 0.3351)	91.1	2393
KSYBO:0.02Eu^{3+}, 0.05Li^+	(0.5816, 0.3447)	93.4	2444
KSYBO:0.02Eu^{3+}, 0.05Na^+	(0.6132, 0.3407)	97.7	2253

and field asymmetry.

Furthermore, the chromaticity coordinates of Li^+ co-doped samples suggest a shift not only in hue but also in color purity, possibly due to localized field distortions that selectively amplify electric dipole transitions. Taken together, these findings reveal a direct correlation between local structural perturbations, forbidden transition activation, and chromaticity variation. Li^+ and Na^+ ions function as structural field modifiers, with Li^+ producing stronger asymmetry capable of activating electric dipole transitions typically inaccessible in centrosymmetric environments. This effect is visibly reflected in both the PL spectra and chromaticity diagrams, underscoring the structural sensitivity of Eu^{3+} emission in borate hosts.

While the observed ~58-fold enhancement in the $^5D_0 \rightarrow {}^7F_4$ transition and the elevated Judd–Ofelt Ω_6 parameter provide compelling evidence for symmetry breaking, the exclusive attribution to static lattice distortion may overlook dynamic factors that can also perturb parity selection rules. In particular, vibronic coupling and phonon-assisted mixing of 4f and higher electronic states may contribute significantly to the activation of nominally forbidden transitions. Furthermore, the

absence of detailed site occupancy analysis limits insight into the specific crystallographic role of Li^+ and Na^+ ions. Given the smaller radius and higher field polarizability of Li^+, its potential preference for interstitial or distorted Y^{3+} sites may amplify the local electric field asymmetry—accounting for both the enhanced electric dipole transition probability and the anomalous branching behavior. This notion is supported by the unusually high Ω_6 value (5.42×10^{-20} cm^2), rarely observed in structurally rigid borates. Finally, while the thermal stability enhancement through Li^+ doping is quantified via activation energy ($E_a = 0.190$ eV), a comparative analysis with related borate-based phosphors suggests that this stabilization is likely due not only to suppression of non-radiative phonon interactions but also to increased lattice rigidity induced by aliovalent substitution. Future studies incorporating DFT modeling or EXAFS analysis could elucidate the local structural rearrangements responsible for these effects.

4. Conclusion

In this work, Eu^{3+}-activated $K_7SrY_2(B_5O_{10})_3$ (KSYBO) phosphors were successfully synthesized via a solid-state reaction method, and the influence of alkali ion co-doping—particularly Li^+—on their structural and optical properties was systematically investigated. Structural characterization confirmed phase-pure trigonal symmetry with homogeneous Eu^{3+} incorporation and no secondary phases, while vibrational (FTIR/Raman) analysis revealed subtle but significant local distortions upon Li^+ co-doping. Crucially, Li^+ addition was found to drastically break local symmetry, resulting in a remarkable enhancement (nearly ~58-fold) in the intensity of the parity-forbidden $^5D_0 \rightarrow {}^7F_4$ transition. This anomalous behavior is strongly supported by Judd–Ofelt analysis, which yielded an exceptionally high Ω_6 parameter (5.42×10^{-20} cm^2), validating the emergence of pronounced electric dipole contributions due to structural asymmetry. Specifically, the Ω_6/Ω_2 ratio could be proposed as a diagnostic metric to forecast the dominance of the $^7F_4$ emission band over the conventionally intense $^7F_2$ transition in Eu^{3+}-activated hosts, enabling rational design of tailored photonic materials. Furthermore, CIE chromaticity analysis revealed a shift toward deeper red hues and broader color distribution in Li^+-modified samples. The co-doped compositions also demonstrated significantly improved thermal stability, with an activation energy of 0.190 eV—surpassing many benchmarks for Eu^{3+}-doped red phosphors. Time-resolved photoluminescence measurements confirmed prolonged lifetimes, further validating the suppression of non-radiative decay pathways. Overall, this study reveals that Li^+-induced symmetry engineering is a powerful strategy to activate otherwise forbidden transitions, enhance radiative dynamics, and improve colorimetric and thermal performance. This is further supported by CIE-based chromaticity analysis, which revealed significantly enhanced color purity (up to 97.7 %) and reduced correlated color temperatures (as low as 2253 K), reinforcing the role of Li^+ in optimizing red emission characteristics. Building on the observed thermal robustness and favorable chromaticity behavior, the KSYBO:Eu^{3+}, Li^+ phosphor not only emerges as a promising candidate for warm white pc-WLEDs but also holds potential for specialized applications such as horticultural lighting. The emission proximity to the photosynthetically active red spectral window (~620–700 nm) suggests further functional optimization toward plant-growth-enhancing lighting systems. These results position KSYBO:Eu^{3+},Li^+ phosphors as structurally responsive, high-efficiency candidates for phosphor-converted white LED (pc-WLED) applications and pave the way for designing next-generation red-emitting materials through targeted lattice manipulation.

Declaration of competing interest

The authors declare that they have no known competing financial interests or personal relationships that could have appeared to influence the work reported in this paper.

Acknowledgements

We would like to express our sincere gratitude to the Princess Nourah bint Abdulrahman University Researchers Supporting Project (Project No. PNURSP2025R16), Princess Nourah bint Abdulrahman University, Riyadh, Saudi Arabia. This study was also financially supported by the Scientific and Technological Research Council of Turkey (TÜBİTAK, Project No. 223M036).

Data availability

Data will be made available on request.

References

[1] G. Blasse, B.C. Grabmaier, Luminescent Materials, Springer Berlin Heidelberg, Berlin, Heidelberg, 1994, https://doi.org/10.1007/978-3-642-79017-1.
[2] K. Binnemans, Lanthanide-based luminescent hybrid materials, Chem. Rev. 109 (2009) 4283–4374, https://doi.org/10.1021/cr8003983.
[3] J. Shen, L.-D. Sun, C.-H. Yan, Luminescent rare earth nanomaterials for bioprobe applications, Dalton Trans. (2008) 5687, https://doi.org/10.1039/b805306e.
[4] X. Huang, B. Li, H. Guo, Highly efficient Eu^{3+}-activated $K_2Gd(WO_4)(PO_4)$ red-emitting phosphors with superior thermal stability for solid-state lighting, Ceram. Int. 43 (2017) 10566–10571, https://doi.org/10.1016/j.ceramint.2017.05.123.
[5] A.S. Altowyan, U.H. Kaynar, E.A. Çin, T. Karaman, H. Aydin, M.B. Coban, J. Hakami, N. Can, Eu^{3+} and Li^+ co-doped $SmCa_4O(BO_3)_3$ phosphors: negative thermal quenching and photoluminescence properties, J. Alloys Compd. 1021 (2025) 179766, https://doi.org/10.1016/j.jallcom.2025.179766.
[6] A.A. Kaminskii, Laser Crystals: Their physics and properties, second ed, Springer Berlin Heidelberg, Berlin, Heidelberg, 1990, https://doi.org/10.1007/978-3-540-70749-3.
[7] Z. Li, P. Wu, X. Jiang, Z. Zhang, S. Xu, The synthesis of rare earth borate glasses and their luminescence properties, JOL 40–41 (1988) 135–136, https://doi.org/10.1016/0022-2313(88)90124-X.
[8] S.P. Jambhale, M.P. Palan, C.B. Hargunani, A comprehensive review on rare earth activated borate phosphors: synthesis, properties, and applications, Int. J. Sci. Res. Sci. Technol. 12 (2025) 204–208.
[9] S. Srivastava, S.K. Behera, B.B. Nayak, Photoluminescence characteristics and white light generation in borohydride derived co-doped (Eu^{3+}, Tb^{3+}) YBO3 phosphors, Optik 231 (2021) 166411, https://doi.org/10.1016/j.ijleo.2021.166411.
[10] P. Wu, X. Tong, Y. Xu, J. Han, H.J. Seo, X. Zhang, Investigation of site occupancy and photoluminescence of Ce^{3+} in cubic borate $Ba_3Y_2(B_2O_5)_3$ and $Ce^{3+} \rightarrow Tb^{3+}$ energy transfer behavior, Opt. Mater. 91 (2019) 246–252, https://doi.org/10.1016/j.optmat.2019.03.030.
[11] M. Behera, R. Panda, R. Arun Kumar, P. Wozny, N.K. Mishra, K. Kumar, M. Runowski, Highly saturated red-emitting novel europium doped yttrium calcium borate (Eu^{3+}:$Y_2CaB_{10}O_{19}$) phosphor materials for eco-friendly solid-state lighting applications, J. Alloys Compd. 1006 (2024) 176294, https://doi.org/10.1016/j.jallcom.2024.176294.
[12] M. Mutailipu, K.R. Poeppelmeier, S. Pan, Borates: a rich source for optical materials, Chem. Rev. 121 (2021) 1130–1202, https://doi.org/10.1021/acs.chemrev.0c00796.
[13] X. Chen, Y. Li, J. Luo, S. Zhao, Recent advances in non-π-conjugated nonlinear optical sulfates with deep-UV absorption edge, Chinese J. Struct. Chem. 42 (2023) 100044, https://doi.org/10.1016/j.cjsc.2023.100044.
[14] A.Y. Jamous, V.A. Svetlichnyi, A.B. Kuznetsov, K.A. Kokh, N.G. Kononova, I. N. Lapin, A. Bolatov, Y.A. Zholdas, A.E. Kokh, Linear and nonlinear optical properties of trigonal borate crystals $K_7MIn_{2-x}Yb_x(B_5O_{10})_3$ (M = Ca, Sr, Ba; x = 0…2) with isolated B_5O_{10} units, J. Alloys Compd. 935 (2023) 167912, https://doi.org/10.1016/j.jallcom.2022.167912.
[15] A.B. Kuznetsov, D.M. Ezhov, K.A. Kokh, N.G. Kononova, V.S. Shevchenko, S. V. Rashchenko, E.V. Pestryakov, V.A. Svetlichnyi, I.N. Lapin, A.E. Kokh, Flux growth and optical properties of $K_7CaY_2(B_5O_{10})_3$ nonlinear crystal, Mater. Res. Bull. 107 (2018) 333–338, https://doi.org/10.1016/j.materresbull.2018.07.037.
[16] S. Zhao, G. Zhang, J. Yao, Y. Wu, $K_6Li_3Sc_2B_{15}O_{30}$: a new nonlinear optical crystal with a short absorption edge, CrystEngComm 14 (2012) 5209, https://doi.org/10.1039/c2ce25304f.
[17] D. Zhao, F.-X. Ma, R.-J. Zhang, M. Huang, P.-F. Chen, R.-H. Zhang, W. Wei, Substitution disorder and photoluminescent property of a new rare-earth borate: $K_3TbB_6O_{12}$, Zeitschrift Für Krist. - Cryst. Mater. 231 (2016) 525–530, https://doi.org/10.1515/zkri-2016-1959.
[18] D. Zhao, F.-X. Ma, Z.-Q. Wu, L. Zhang, W. Wei, J. Yang, R.-H. Zhang, P.-F. Chen, S.-X. Wu, Synthesis, crystal structure and characterizations of a new red phosphor $K_3EuB_6O_{12}$, Mater. Chem. Phys. 182 (2016) 231–236, https://doi.org/10.1016/j.matchemphys.2016.07.027.
[19] R.K. Li, C.C. Wu, M.J. Xia, $LiCaTb_5(BO_3)_6$: a new magneto-optical crystal promising as faraday rotator, Opt. Mater. 62 (2016) 452–457, https://doi.org/10.1016/j.optmat.2016.10.025.
[20] Y. Gao, C. Yin, P. Jiang, W. Gao, R. Cong, T. Yang, Synthesis, crystal structure of $LiCaRE_5(BO_3)_6$ (RE = Sm, Eu, Gd, Tb, Dy, Ho, Er, Tm, Yb, Lu, Y) and Eu^{3+}

luminescence in $LiCaRE_5(BO_3)_6$ (RE = Gd, Y, Lu), J. Solid State Chem. 293 (2021) 121821, https://doi.org/10.1016/j.jssc.2020.121821.
[21] Y. Gao, X. Zhu, H. Shi, P. Jiang, R. Cong, T. Yang, Eu^{3+} and Tb^{3+} doped $LiCaY_5(BO_3)_6$: efficient red and green phosphors under UV or NUV excitations, JOL 242 (2022) 118598, https://doi.org/10.1016/j.jlumin.2021.118598.
[22] S.C. Kaynar, A.S. Altowyan, H. Aydin, U.H. Kaynar, M.B. Coban, J. Hakami, N. Can, Judd–Ofelt analysis and photoluminescence behavior of Tb^{3+}-activated $K_7SrY_2(B_5O_{10})_3$ phosphors modified with alkali co-dopants for solid-state lighting applications, Spectrochim. Acta Part A Mol. Biomol. Spectrosc. 341 (2025) 126435, https://doi.org/10.1016/j.saa.2025.126435.
[23] A.B. Kuznetsov, Y.A. Zholdas, L.A. Gorelova, A.D. Fedorenko, A.A. Ryadun, Y. V. Seryotkin, V.S. Shevchenko, A.E. Kokh, A.O. Klimov, K.A. Kokh, Synthesis, growth, and luminescence properties of rare earth borates $KSrY(BO_3)_2$:Tb^{3+} and Tb^{4+}, Cryst. Growth Des. 24 (2024) 5478–5485, https://doi.org/10.1021/acs.cgd.4c00140.
[24] D.A.E. Somaily, A.S. Altowyan, U.H. Kaynar, H. Aydin, J. Hakami, M.B. Coban, T. Zelai, N. Can, Tunable luminescence and structural modifications in Eu^{3+}/Li^+ Co-doped $YBa_3(BO_3)_3$ phosphors for LEDs, Mater. Res. Bull. 189 (2025) 113453, https://doi.org/10.1016/j.materresbull.2025.113453.
[25] A.S. Altowyan, U.H. Kaynar, H. Aydin, M.B. Coban, Z.G. Portakal, S. Akça-Özalp, J. Hakami, M. Ayvacikli, M. Topaksu, N. Can, Enhanced photoluminescence properties of Eu^{3+}/Li^+ co-doped ZrO_2: a focus on red and far-red emissions, J. Photochem. Photobiol. A Chem. 466 (2025) 116408, https://doi.org/10.1016/j.jphotochem.2025.116408.
[26] V.R. Mala, P. Balakrishnan, S.M. Moses Kennedy, Influence of co-doping alkali metal ions $Li^+/Na^+/K^+$ on the luminescence enhancement properties of the red emitting $Ba_2CaZn_2Si_6O_{17}$:Eu^{3+} phosphor along with the optical transition probabilities by Judd-Ofelt analysis for solid state lighting applications, Opt. Mater. 159 (2025) 116672, https://doi.org/10.1016/j.optmat.2025.116672.
[27] X. Gao, W. Zhang, X. Wang, X. Huang, Z. Zhao, Charge compensation effects of alkali metal ions M^+ (Li^+, Na^+, K^+) on luminescence enhancement in red-emitting $Ca_3Si_2O_7$:Eu^{3+} phosphors, J. Alloys Compd. 893 (2022) 162265, https://doi.org/10.1016/j.jallcom.2021.162265.
[28] F. Auzel, Upconversion processes in coupled ion systems, JOL 45 (1990) 341–345, https://doi.org/10.1016/0022-2313(90)90189-I.
[29] T. Liu, Q. Meng, W. Sun, Luminescent properties of Eu^{3+} doped $NaY(WO_4)_2$ nanophosphors prepared by molten salt method, J. Rare Earths 33 (2015) 915–921, https://doi.org/10.1016/S1002-0721(14)60505-6.
[30] Q. Sun, R.-Q. Piao, Y. Wang, Z.-B. Zhang, D.-L. Zhang, Optical and Judd-Ofelt spectroscopic study of Er^{3+}/Pr^{3+}-codoped $Gd_3Ga_5O_{12}$ crystal, J. Alloys Compd. 783 (2019) 836–840, https://doi.org/10.1016/j.jallcom.2018.12.360.
[31] K. Wu, Z. Xi, R. Qiu, J. Zhang, Z. Li, Luminescence performance, temperature sensing characteristics and Judd-Ofelt theory analysis of Y_2MoO_6:$Er^{3+}/Yb^{3+}/Li^+$ upconversion phosphors, Ceram. Int. 50 (2024) 53888–53898, https://doi.org/10.1016/j.ceramint.2024.10.241.
[32] R.D. Shannon, Revised effective ionic radii and systematic studies of interatomic distances in halides and chalcogenides, Acta Crystallogr. Sect. A 32 (1976) 751–767, https://doi.org/10.1107/S0567739476001551.
[33] A.M. Pires, M.R. Davolos, Luminescence of europium(III) and manganese(II) in barium and zinc orthosilicate, Chem. Mater. 13 (2001) 21–27, https://doi.org/10.1021/cm000063g.
[34] G. Williamson, W. Hall, X-ray line broadening from filed aluminium and wolfram, Acta Metall. 1 (1953) 22–31, https://doi.org/10.1016/0001-6160(53)90006-6.
[35] B.D. Cullity, S.R. Stock, Elements of X-Ray Diffraction, 3rd Editio, Prentice Hall, 2001.
[36] P. Pascuta, L. Pop, S. Rada, M. Bosca, E. Culea, The local structure of bismuth borate glasses doped with europium ions evidenced by FT-IR spectroscopy, J. Mater. Sci. Mater. Electron. 19 (2008) 424–428, https://doi.org/10.1007/s10854-007-9359-5.
[37] A.S. Oreshonkov, E.M. Roginskii, N.P. Shestakov, I.A. Gudim, V.L. Temerov, I. V. Nemtsev, M.S. Molokeev, S.V. Adichtchev, A.M. Pugachev, Y.G. Denisenko, Structural, electronic and vibrational properties of $YAl_3(BO_3)_4$, Materials 13 (2020) 545, https://doi.org/10.3390/ma13030545.
[38] K. Mariselvam, R. Arun Kumar, M. Jagadeesh, Spectroscopic properties and Judd-Ofelt analysis of Eu^{3+} doped barium bismuth fluoroborate glasses, Opt. Mater. 84 (2018) 427–435, https://doi.org/10.1016/j.optmat.2018.07.044.
[39] W.A. Pisarski, J. Pisarska, W. Ryba-Romanowski, Structural role of rare earth ions in lead borate glasses evidenced by infrared spectroscopy: $BO_3 \leftrightarrow BO_4$ conversion, J. Mol. Struct. 744–747 (2005) 515–520, https://doi.org/10.1016/j.molstruc.2005.01.022.
[40] S.E. Kichanov, Y.E. Gorshkova, G.E. Rachkovskaya, D.P. Kozlenko, G. B. Zakharevich, B.N. Savenko, Structural evolution of luminescence nanoparticles with rare-earth ions in the oxyfluoride glass ceramics, Mater. Chem. Phys. 237 (2019) 121830, https://doi.org/10.1016/j.matchemphys.2019.121830.
[41] J. Gharavi-Naeini, K.W. Yoo, N.A. Stump, Characterization of barium borate frameworks using Raman spectroscopy, Appl. Spectrosc. 72 (2018) 627–633, https://doi.org/10.1177/0003702817748952.
[42] D. Tuschel, Exploring resonance Raman spectroscopy, Spectrosc 33 (2018) 12–19.
[43] P. Marabotti, M. Tommasini, C. Castiglioni, P. Serafini, S. Peggiani, M. Tortora, B. Rossi, A. Li Bassi, V. Russo, C.S. Casari, Electron-phonon coupling and vibrational properties of size-selected linear carbon chains by resonance Raman scattering, Nat. Commun. 13 (2022) 5052, https://doi.org/10.1038/s41467-022-32801-3.
[44] X. Liu, L. Li, H.M. Noh, B.K. Moon, B.C. Choi, J.H. Jeong, Chemical bond properties and charge transfer bands of O^{2-}–Eu^{3+}, O^{2-}–Mo^{6+} and O^{2-}–W^{6+} in Eu^{3+}-doped garnet hosts $Ln_3M_5O_{12}$ and ABO_4 molybdate and tungstate phosphors, Dalton Trans. 43 (2014) 8814, https://doi.org/10.1039/c4dt00674g.
[45] S. Das, S. Som, C.-Y. Yang, S. Chavhan, C.-H. Lu, Structural evaluations and temperature dependent photoluminescence characterizations of Eu^{3+}-activated $SrZrO_3$ hollow spheres for luminescence thermometry applications, Sci. Rep. 6 (2016) 25787, https://doi.org/10.1038/srep25787.
[46] H. Xie, L. Xu, L. Qin, Y. Huang, D. Wei, S. Il Kim, H.J. Seo, Orange-emitting $Ba_4R_2ZrWO_{12}$:Eu^{3+} (R=La, Gd, Y) with the strongest $^5D_0 \rightarrow {}^7F_0$ transition, Mater. Lett. 115 (2014) 18–20, https://doi.org/10.1016/j.matlet.2013.09.105.
[47] M.T. Harrison, R.G. Denning, Site selective spectroscopy and molecular dynamics simulation of Eu(III) ZBLAN glasses, JOL 69 (1996) 265–285, https://doi.org/10.1016/S0022-2313(96)00106-8.
[48] V. Ghenea, I. Culeac, A. Buzdugan, Eu^{3+} As a luminescent probe for local site symmetry in Eu(III) coordination compounds, J. Eng. Sci. 31 (2024) 28–38, https://doi.org/10.52326/jes.utm.2024.31(2).03.
[49] K. Ueda, T. Yoshino, Y. Shimizu, T. Honma, F. Massuyeau, S. Jobic, Site-dependent Eu^{3+} photoluminescence in double perovskite-type alkaline earth lanthanum tantalates, JOL 229 (2021) 117683, https://doi.org/10.1016/j.jlumin.2020.117683.
[50] Y. Kitagawa, J. Ueda, K. Arai, H. Kageyama, S. Tanabe, Difference of Eu^{3+} luminescent properties in YOCl and YOBr oxyhalide hosts, J. Appl. Phys. 129 (2021) 183104, https://doi.org/10.1063/5.0049826.
[51] D.L. Dexter, J.H. Schulman, Theory of concentration quenching in inorganic phosphors, J. Chem. Phys. 22 (1954) 1063–1070, https://doi.org/10.1063/1.1740265.
[52] W. Lenth, G. Huber, D. Fay, Interionic energy transfer by electric multipole interaction in rare-earth pentaphosphates, Phys. Rev. B 23 (1981) 3877–3885, https://doi.org/10.1103/PhysRevB.23.3877.
[53] X. Cheng, D. Tu, W. Zheng, X. Chen, Energy transfer designing in lanthanide-doped upconversion nanoparticles, Chem. Commun. 56 (2020) 15118–15132, https://doi.org/10.1039/D0CC05878E.
[54] U.H. Kaynar, H. Aydin, A.S. Altowyan, J. Hakami, M.B. Coban, M. Ayvacikli, E. Ekdal Karali, A. Canimoglu, N. Can, Enhancement of luminescence and thermal stability in Eu^{3+}-doped $K_3Y(BO_2)_6$ with Li^+ and Na^+ co-doping, Adv. Powder Technol. 35 (2024) 104695, https://doi.org/10.1016/j.apt.2024.104695.
[55] L.G. Van Uitert, Characterization of energy transfer interactions between rare earth ions, J. Electrochem. Soc. 114 (1967) 1048, https://doi.org/10.1149/1.2424184.
[56] P. Ling-Hu, X. Guo, J. Hu, C. Deng, R. Cui, Anomalous $^5D_0 \rightarrow {}^7F_4$ transition of Eu^{3+}-doped BaLaGaO 4 phosphors for WLEDs and plant growth applications, Adv Opt Mater 12 (2024) 2301760, https://doi.org/10.1002/adom.202301760.
[57] M. Zheng, W. Zhang, Q. Ou, J. Tang, Investigation of preparation and photoluminescence properties of europium-doped calcium orthoborate ($Ca_3B_2O_6$:Eu^{3+}) red phosphor and red LED, Ceram. Int. 50 (2024) 53618–53627, https://doi.org/10.1016/j.ceramint.2024.10.211.
[58] T. Sakthivel, G. Annadurai, R. Vijayakumar, X. Huang, Synthesis, luminescence properties and thermal stability of Eu^{3+}-activated $Na_2Y_2B_2O_7$ red phosphors excited by near-UV light for pc-WLEDs, JOL 205 (2019) 129–135, https://doi.org/10.1016/j.jlumin.2018.09.008.
[59] B. Henderson, G.F. Imbusch, Optical Spectroscopy of Inorganic Solids, Oxford University Press, Oxford, 2006, https://doi.org/10.1093/oso/9780199298624.001.0001.
[60] K. Marimuthu, S. Surendra Babu, G. Muralidharan, S. Arumugam, C.K. Jayasankar, Structural and optical studies of Eu^{3+} ions in alkali borate glasses, Phys. Status Solidi 206 (2009) 131–139, https://doi.org/10.1002/pssa.200824198.
[61] Q. Lv, B. Shao, X. Ma, S. Yang, C. Wang, Y. Dong, E. Dong, C. Wang, A novel efficient red-emitting $K_7SrY_2B_{15}O_{30}$:Eu^{3+} phosphor with non-concentration quenching and robust thermal stability for white LEDs, Spectrochim. Acta Part A Mol. Biomol. Spectrosc. 287 (2023) 122126, https://doi.org/10.1016/j.saa.2022.122126.
[62] R. Li, R. Cui, X. Guo, J. Zhang, C. Deng, X. Gong, Thermally-stable novel reddish-orange emitting $Gd_7O_6(BO_3)(PO_4)_2$:Eu^{3+} phosphor for WLEDs, Opt. Mater. 157 (2024) 116014, https://doi.org/10.1016/j.optmat.2024.116014.
[63] G.-H. Li, N. Yang, J. Zhang, J.-Y. Si, Z.-L. Wang, G.-M. Cai, X.-J. Wang, The non-concentration-quenching phosphor $Ca_3Eu_2B_4O_{12}$ for WLED application, Inorg. Chem. 59 (2020) 3894–3904, https://doi.org/10.1021/acs.inorgchem.9b03565.
[64] T. Sakthivel, L. Sun, B. Devakumar, B. Li, X. Huang, Novel high-efficiency Eu^{3+}-activated $Na_2Gd_2B_2O_7$ red-emitting phosphors with high color purity, RSC Adv. 8 (2018) 32948–32955, https://doi.org/10.1039/C8RA06607H.
[65] B.R. Judd, Optical absorption intensities of rare-earth ions, Phys. Rev. 127 (1962) 750–761, https://doi.org/10.1103/PhysRev.127.750.
[66] G.S. Ofelt, Intensities of crystal spectra of rare-earth ions, J. Chem. Phys. 37 (1962) 511–520, https://doi.org/10.1063/1.1701366.
[67] W.T. Carnall, P.R. Fields, K. Rajnak, Electronic Energy Levels in the Trivalent Lanthanide Aquo Ions. I. Pr^{3+}, Nd^{3+}, Pm^{3+}, Sm^{3+}, Dy^{3+}, Ho^{3+}, Er^{3+}, and Tm^{3+}, J. Chem. Phys. 49 (1968) 4424–4442, https://doi.org/10.1063/1.1669893.
[68] P. Dorenbos, The 5d level positions of the trivalent lanthanides in inorganic compounds, JOL 91 (2000) 155–176, https://doi.org/10.1016/S0022-2313(00)00229-5.
[69] N. Luewarasirikul, J. Kaewkhao, Spectroscopic properties and Judd-Ofelt analysis of Eu^{3+} doped Ba-Na-B glasses for photonic applications, J. Phys. Conf. Ser. 1819 (2021) 012072, https://doi.org/10.1088/1742-6596/1819/1/012072.
[70] F. Du, Y. Nakai, T. Tsuboi, Y. Huang, H.J. Seo, Luminescence properties and site occupations of Eu^{3+} ions doped in double phosphates $Ca_9R(PO_4)_7$ (R = Al, Lu), J. Mater. Chem. 21 (2011) 4669, https://doi.org/10.1039/c0jm03324c.

[71] X. Liu, C. Li, Z. Quan, Z. Cheng, J. Lin, Tunable luminescence properties of $CaIn_2O_4:Eu^{3+}$ phosphors, J. Phys. Chem. C 111 (2007) 16601–16607, https://doi.org/10.1021/jp074868o.
[72] Y.-C. Chang, C.-H. Liang, S.-A. Yan, Y.-S. Chang, Synthesis and photoluminescence characteristics of high color purity and brightness $Li_3Ba_2Gd_3(MoO_4)_8:Eu^{3+}$ red phosphors, J. Phys. Chem. C 114 (2010) 3645–3652, https://doi.org/10.1021/jp9084124.
[73] R. Nagaraj, A. Raja, S. Ranjith, Synthesis and luminescence properties of novel red-emitting Eu^{3+} ions doped silicate phosphors for photonic applications, J. Alloys Compd. 827 (2020) 154289, https://doi.org/10.1016/j.jallcom.2020.154289.
[74] J. Luo, Y. Wang, S. Chen, S. Li, Y. Zhao, J. Chen, Z. Hu, Y. Li, H. Wang, R. Yu Bin Deng, Surface modification of $Mg_2InSbO_6:Eu^{3+}$ phosphors and applications for white light-emitting diodes and visualization of latent fingerprint, J. Alloys Compd. 892 (2022) 162049, https://doi.org/10.1016/j.jallcom.2021.162049.
[75] G. Zhu, Z. Ci, Y. Shi, M. Que, Q. Wang, Y. Wang, Synthesis, crystal structure and luminescence characteristics of a novel red phosphor $Ca_{19}Mg_2(PO_4)_{14}:Eu^{3+}$ for light emitting diodes and field emission displays, J. Mater. Chem. C 1 (2013) 5960, https://doi.org/10.1039/c3tc31263a.
[76] N. Singkiburin, N. Srisittipokakun, N. Kiwsakunkran, R. Rajaramakrishna, C. S. Sarumaha, W. Busayaporn, A. Angnanon, N. Intachai, S. Kothan, H.J. Kim, J. Kaewkhao, Influence of asymmetry around Eu^{3+} ion on luminescence behaviours of ZnO–Na2O–B2O3 glasses synthesized by microwave and conventional melting methods: red emitting material application, Radiat. Phys. Chem. 237 (2025) 113082, https://doi.org/10.1016/j.radphyschem.2025.113082.
[77] J. Zhou, Z. Xia, Luminescence properties and energy transfer studies of a color tunable $BaY_2Si_3O_{10}:Tm^{3+},Dy^{3+}$ phosphor, Opt. Mater. 53 (2016) 116–122, https://doi.org/10.1016/j.optmat.2016.01.023.
[78] B.M. Thammanna, K. Viswanathan, H.P. Nagaswarupa, K.R. Vishnumahesh, Novel $MgTiO_3:Eu^{3+}$ nanophosphor its photometric analysis for multifunctional applications, Mater Today Proc 4 (2017) 12306–12313, https://doi.org/10.1016/j.matpr.2017.09.164.